MCB
Journals.ASM.org

# Miro-1 Links Mitochondria and Microtubule Dynein Motors To Control Lymphocyte Migration and Polarity

**Giulia Morlino,[a,b] Olga Barreiro,[a,b] Francesc Baixauli,[a,b] Javier Robles-Valero,[c] José M. González-Granado,[a] Ricardo Villa-Bellosta,[d] Jesús Cuenca,[e] Carlos O. Sánchez-Sorzano,[e] Esteban Veiga,[f,g] Noa B. Martín-Cófreces,[a,b] Francisco Sánchez-Madrid[a,b]**

Vascular Biology and Inflammation Department, Centro Nacional Investigaciones Cardiovasculares, Madrid, Spain[a]; Servicio de Inmunologia, Instituto Investigación Sanitaria Princesa, Madrid, Spain[b]; Centro de Investigación del Cáncer, CSIC-Universidad de Salamanca, Salamanca, Spain[c]; Department of Epidemiology Atherothrombosis and Imaging, Centro Nacional de Investigaciones Cardiovasculares, Madrid, Spain[d]; Unidad de Biocomputación, Centro Nacional de Biotecnología (CSIC), Universidad Autónoma de Madrid, Madrid, Spain[e]; Departamento de Biología Molecular y Celular, Centro Nacional de Biotecnología, CSIC, Madrid, Spain[f]; Unidad de Investigación, Hospital Santa Cristina, Madrid, Spain[g]

**The recruitment of leukocytes to sites of inflammation is crucial for a functional immune response. In the present work, we explored the role of mitochondria in lymphocyte adhesion, polarity, and migration. We show that during adhesion to the activated endothelium under physiological flow conditions, lymphocyte mitochondria redistribute to the adhesion zone together with the microtubule-organizing center (MTOC) in an integrin-dependent manner. Mitochondrial redistribution and efficient lymphocyte adhesion to the endothelium require the function of Miro-1, an adaptor molecule that couples mitochondria to microtubules. Our data demonstrate that Miro-1 associates with the dynein complex. Moreover, mitochondria accumulate around the MTOC in response to the chemokine CXCL12/SDF-1α; this redistribution is regulated by Miro-1. CXCL12-dependent cell polarization and migration are reduced in Miro-1-silenced cells, due to impaired myosin II activation at the cell uropod and diminished actin polymerization. These data point to a key role of Miro-1 in the control of lymphocyte adhesion and migration through the regulation of mitochondrial redistribution.**

The recruitment of blood leukocytes to the site of inflammation involves a sequential, multistep adhesion cascade between the leukocyte and endothelial cell adhesion molecules that mediates leukocyte rolling, firm adhesion, and transmigration across the endothelium (1). Firm arrest of leukocytes on endothelial cells is mediated by the interaction of leukocyte integrins, mainly very late antigen 4 (VLA-4) (α4β1) and lymphocyte function-associated antigen 1 (LFA-1) (αLβ2), with their respective endothelial counterreceptors vascular cell adhesion molecule 1 (VCAM-1) and intercellular adhesion molecule 1 (ICAM-1) (2). During this process, the leukocyte and endothelium cytoskeletons undergo an extensive reorganization that ensures sufficient duration of the contact and enables leukocyte extravasation. Leukocyte navigation through tissues is governed by extracellular signals, such as chemoattractant gradients (chemotaxis) and adhesion signals. Chemokines, by activating specific receptors of the G-protein-coupled receptor (GPCR) family, generate leukocyte polarity by inducing the formation of a leading edge (through actin polymerization) and a uropod, a slender posterior appendage characterized by actin-myosin-driven contraction (3, 4).

Mitochondria are highly dynamic organelles that continuously remodel their shape and size through fission and fusion events. They are actively relocalized within the cell through a cytoskeleton-based transportation system (5). These organelles move along microtubules in both anterograde and retrograde directions, using kinesin and dynein motor proteins, respectively (6). Specific subcellular locations with high energy and $Ca^{2+}$-buffering requirements, such as cellular synapses and other polarized structures, require the establishment of a high local density of mitochondria (7, 8). In leukocytes, mitochondria relocalize to the uropod during chemotaxis (9) and to the immune synapse (IS) to enable modulation of its architecture and downstream signaling (10–12). The molecular mechanisms driving this mitochondrial positioning to specific subcellular locations in lymphocytes are, however, not well understood.

It has been reported that the atypical Rho GTPase Miro-1 plays an essential role in the regulation of mitochondrial morphogenesis and trafficking along microtubules (13, 14) and might serve as a calcium-dependent sensor for the control of mitochondrial motility (15–17). Miro-1 binds the cytoplasmic adaptor protein milton and kinesin heavy chain through its cytoplasmic domains, thereby connecting mitochondria to microtubules (18). Miro-1 contains a transmembrane domain that anchors it to the outer mitochondrial membrane, two GTPase domains, and two $Ca^{2+}$-sensing EF-hand domains that protrude into the cytoplasm (14). Upon binding of $Ca^{2+}$ to its EF-hand domains, Miro-1 dissociates from microtubules (19). The expression of a Miro-1 form with a double mutation in its EF-hands prevents the arrest of mitochondria in response to cytoplasmic $Ca^{2+}$ elevation (15–17) and decreases the level of $Ca^{2+}$ entering mitochondria (20).

Here we show that the lymphocyte mitochondria specifically redistribute to the adhesion zone in close contact with the endothelium. Our results indicate that Miro-1, through the regulation of mitochondrial movement along microtubules and its associa-

**Received** 5 September 2013 **Returned for modification** 25 October 2013
**Accepted** 24 January 2014
**Published ahead of print** 3 February 2014

Address correspondence to Francisco Sánchez-Madrid, fsmadrid@salud.madrid.org.

Supplemental material for this article may be found at http://dx.doi.org/10.1128/MCB.01177-13.

doi:10.1128/MCB.01177-13

tion with dynein/dynactin motors, influences mitochondrial positioning. Deficiency in Miro-1 prevents correct interaction with inflamed endothelium, lymphocyte polarization, and chemotactic migration.

(Giulia Morlino conducted this study in partial fulfillment of the requirements for a Ph.D. in Molecular Medicine, Program in Basic and Applied Immunology, San Raffaele University, Milan, Italy.)

## MATERIALS AND METHODS

**Cells, plasmids, and cell transfection.** Human umbilical vein endothelial cells (HUVEC) were obtained and cultured as previously described (21). To activate HUVEC, tumor necrosis factor alpha (TNF-α) (20 ng/ml; R&D Systems) was added to the culture medium 20 h before adhesion/migration assay. Human peripheral blood lymphocytes (PBLs) and T lymphoblasts were obtained and cultured as described elsewhere (22). CEM T cells, CH7C17 T cells, and the human erythroleukemic cell line K562 stably overexpressing α4 or αL integrin were grown in RPMI 1640 medium (GIBCO BRL) supplemented with 10% fetal calf serum (FCS) (Invitrogen), 50 IU/ml penicillin, and 50 μg/ml streptomycin. Medium for CH7C17 cells was further supplemented with 400 μg/ml hygromycin B and 4 μg/ml puromycin, and medium for K562 was further supplemented with 1 mg/ml G418. The HEK293T cell line was cultured in Dulbecco modified Eagle medium (DMEM) (Sigma) supplemented with 10% FCS.

Plasmids encoding fluorescence-tagged ICAM-1 proteins (green fluorescent protein [GFP], yellow fluorescent protein [YFP], and cyan fluorescent protein [CFP]) were described previously (23). Plasmids encoding mitochondrion-targeted dsRED (mtRFP) or mtYFP (24) were generously provided by L. Scorrano (University of Padua, Italy). The EB1-GFP construct was a kind gift from Anna Akhmanova (Utrecht University, The Netherlands). The GFP-Miro construct was a gift from J. T. Kittler (University College London); the double K208 K328 Miro-1 mutation (Miro-$1^{KK}$) was generated by site-directed mutagenesis with the QuikChange protocol (Stratagene). Small interfering RNAs (siRNAs) against human dynein heavy chain (DHC) were previously described (25); those against Miro-1 were a SMARTpool of 4 distinct siRNAs (5′-GCUUAAUCGUAGCUGCAAA-3′, 5′-CCAGAGAGGGAGACACGAA-3′, 5′-GCAAUUAGCAGAGGCGUUA-3′, and 5′-UGUGGAGUGUUCAGCGAAA-3′) obtained, together with the negative-control siRNA (5′-AAUUCUCCGAACGUGUCACGUdTdT-3′), from Thermo Scientific Dharmacon. T-cell lines, human T lymphoblasts, and HUVEC were transfected with DNA plasmids or with specific double-stranded siRNAs by electroporation using the Gene Pulser II electroporation system (Bio-Rad Laboratories) or the Nucleofector system (Amaxa Biosystems). HEK293T cells were transfected using Lipofectamine (Invitrogen). CEM T cells were electroporated twice (at 0 and 72 h) with specific siRNA at a final concentration of 2 μM. The efficiency of gene silencing was checked by Western blotting, and cells were used for experiments on day 6 after the first electroporation. Transiently transfected HUVEC were used at 24 to 48 h after transfection.

**Reagents and antibodies.** Recombinant human fibronectin (FN), poly-L-lysine (PLL), human gamma globulin, oligomycin, fluorescein isothiocyanate (FITC)-conjugated or unconjugated anti-α-tubulin, and anti-DHC (clone 440) were from Sigma-Aldrich. The mitochondrial calcium uptake inhibitor Ru360 and antibiotic G418 were from Calbiochem. The fluorescent cell tracker BCECF-AM, Alexa Fluor 488, and 647 phalloidin conjugates, JC-1, Fluo4-AM, Mitotracker Orange, Mitotracker Green, DiO, DiD, and Dil Vybrant cell labeling solutions, and all fluorochrome-conjugated secondary antibodies were from Invitrogen. Puromycin was from InvivoGen and hygromycin B from Roche. PureCol (Advanced BioMatrix) (3 mg ml$^{-1}$) and bovine collagen I (GIBCO) were employed for standard collagen assays and for collagen titration experiments, respectively. The antibodies D3/9 (anti-CD45), HP 2/6 (anti-CD4), HP2/1 (anti-α4 integrin), and TS1/11 (anti-αL integrin) were produced in our laboratory (23). TP 1/25 (anti-ICAM-3) and TS2/16 (anti-β1 integrin) antibodies were described previously (21, 26). Hu5/3 antibody (anti-ICAM-1) was kindly provided by F. W Luscinskas (Brigham and Women Hospital, Boston, MA). Polyclonal antibody against ezrin/moesin (90/3) was provided by Heinz Furthmayr (Stanford University, Stanford, CA). The rabbit polyclonal anti-Mn-superoxide dismutase (anti-MnSOD) antibody was from Rockland. Anti-extracellular signal-regulated kinase 1/2 (anti-ERK1/2) and anti-p74 were from Millipore; phospho-ERK1/2 and anti-pSer19 myosin light chain (MLC) were from Cell Signaling Technology; monoclonal p50-dynamitin, anti-p150$^{glued}$, and anti-CXCR-4 were from BD Transduction Laboratories; and anti-GFP was from Living Colors (Clontech Laboratories, Inc.). Anti-Miro-1 for Western blotting was from Abnova and that for immunoprecipitation (IP) from Abcam. Anti-dynein heavy chain antibody was from Santa Cruz. Antigiantin was from Abcam. Horseradish peroxidase (HRP)-conjugated secondary antibodies were from Pierce. Recombinant human CXCL12 was from ImmunoTools. Integrin inhibitors BIO5192 and BIRT377 were provided by Biogen Idec and Boehringer Ingelheim, respectively (27).

**Fluorescence confocal microscopy.** For immunofluorescence assays, lymphocytes were plated on slides coated with PLL or FN or on confluent HUVEC for 20 min at 37°C, fixed with 4% paraformaldehyde (PFA) (Electron Microscopy Sciences), stained with the indicated antibodies, and mounted in Prolong (Invitrogen). Where indicated, the PLL or FN matrix included 10 nM CXCL12. To detect intracellular proteins, cells were permeabilized for 3 min with 0.2% Triton X-100 in phosphate-buffered saline (PBS) before staining. Confocal images were obtained with a Leica TCS-SP5 confocal scanning laser unit with an inverted epifluorescence microscope (DMI6000B). Microscopes were maintained at 37°C with 5% $CO_2$ and covered by a full acrylic box, allowing live-cell imaging. For time-lapse fluorescence imaging, cells were plated onto coated 35-mm dishes (MatTek).

Redistribution of lymphocyte mitochondria toward the endothelium was calculated as percentage of the fluorescence intensity (FI) of lymphocyte mitochondria located in the third of the cell near the HUVEC contact area. FI was measured using ImageJ or Metamorph. Cellular polarity was assessed by the elliptical form factor, calculated from images with membrane protein staining using Metamorph software. The phosphorylated myosin light-chain (pMLC) concentration at the uropod with respect to the leading edge and the three-dimensional distance between the mitochondrial network and the microtubule-organizing center (MTOC) were quantified using the Fluorescence Ratio and Distance Measure plug-ins for ImageJ, respectively.

**Calcium measurement.** For measurement of intracellular $Ca^{2+}$ flux, control and Miro-1-silenced CEM cells were preincubated with DiD and Dil, respectively, to distinguish them. The pooled cells were loaded with Fluo-4-AM (12) and settled onto MatTek glass-bottom dishes covered by a TNF-α-activated HUVEC monolayer. Images were acquired every 10 s, using a TCS SP5 confocal microscope. The mean Fluo-4 fluorescence intensity of each migrating cell in each frame was calculated by Wimasis GmbH. Calcium peak intensity was calculated by subtracting the basal fluorescence intensity from the maximum fluorescence registered in each peak. Peak duration was calculated by multiplying the number of frames in which it was registered by frame duration in seconds.

**Fluorescence image analysis.** Images were analyzed with Leica LASAF (Leica Microsystems), Metamorph (Universal Imaging Corporation, Downingtown, PA), or ImageJ (NIH) software. Mitochondria and MTOC three-dimensional (3D) reconstructions were obtained using Imaris 7.6 software (Bitplane).

**Fluorescence ratios.** To measure the relative fluorescence between two regions, we computed the ratio between the average fluorescence in the two areas corrected for background fluorescence according to the following model. The model assumes that the observed fluorescence in the different areas can be modeled as the contribution of background fluorescence (Bg), fluorescence in region of interest A ($A$), and fluorescence in region of interest B ($B$):

$$\begin{pmatrix} \mathrm{Bg}_{\mathrm{obs}} \\ A_{\mathrm{obs}} \\ B_{\mathrm{obs}} \end{pmatrix} = \begin{pmatrix} 1 & 0 & 0 \\ 1 & 1 & 1 \\ 1 & 0 & 1 \end{pmatrix} \begin{pmatrix} \mathrm{Bg} \\ A \\ B \end{pmatrix}$$

In the model, fluorescence observed in region A is the sum of the background fluorescence and the fluorescences of regions A and B, while the fluorescence observed in region B is the contribution of the background fluorescence and the fluorescence of region B.

Background-corrected contributions can be estimated by inverting the model:

$$\begin{pmatrix} \mathrm{Bg} \\ A \\ B \end{pmatrix} = \begin{pmatrix} 1 & 0 & 0 \\ 0 & 1 & -1 \\ -1 & 0 & 1 \end{pmatrix} \begin{pmatrix} \mathrm{Bg}_{\mathrm{obs}} \\ A_{\mathrm{obs}} \\ B_{\mathrm{obs}} \end{pmatrix}$$

Note that the estimated $A$ and $B$ have already been corrected for the background fluorescence and that $A$ no longer has a contribution from region B (it is the pure contribution of region A). Finally, we compute the relative fluorescence ratio as $r = (A + B)/B$.

**Distance measurements.** To measure the distance between two three-dimensional fluorescence distributions in independent channels, we binarized both gray-scale stacks (the user can select two thresholds so that the region of interest is isolated in both channels). We then computed the Euclidean distance between every possible pair of voxels (one in distribution A and the other in distribution B). This gives us the exact distribution of pairwise distances. Note that the calculation is fully computed in 3D and therefore that the actual distance between the two regions of interest is calculated. Finally, we computed a truncated mean by computing the distance mean after discarding the 5% lower and upper values. This mean is known to be a robust estimate of the distribution mean.

**TIRFM.** For total internal reflection fluorescence microscopy (TIRFM), control and Miro-1-silenced CEM cells, transfected with EB1-mGFP, were sorted to warrant transfection and cultured for 24 h. Cells were allowed to settle onto FN-coated glass-bottom microwell dishes (no. 1.5; Mattek, Ashland, MA, USA). Recording was initiated 3 min after cell plating, and cells were visualized with a Leica AM TIRF MC M mounted on a Leica DMI 6000B microscope coupled to an Andor-DU8285_VP-4094 camera. Images were acquired with an HCX PL APO 100.0×1.46 oil objective and processed with the accompanying confocal software (LCS; Leica) as described previously (28). For EB1-GFP microtubule plus tip tracking, penetrance was 150 nm for the 488-nm laser channel with same objective angle and a 0.26-s exposure time. Synchronization was performed through the Leica software. Images were analyzed and converted into movies using Imaris software (Bitplane, Switzerland). Quantification of the number of microtubule nucleation events, tracking of microtubule movement trajectories, and computation of microtubule growth were performed with the "connected components" algorithm for particle tracker. EB1-GFP comets were detected by the surface algorithm detection based on channel intensity and using a local background. Analysis was conducted on movie lengths of 300 s that were captured at a rate of 0.5 frame/s. To exclude microtubules that move in and out of the $z$ plane, events shorter than 2 μm were not incorporated into the final analysis.

**Ligand-coated microspheres.** Styrene divinylbenzene latex beads (6-μm diameter; Sigma) were coated with VCAM-1-Fc or ICAM-1-Fc, produced in our laboratory (29). CH7C17 cells preloaded with Mitotracker Orange ($2 \times 10^5$) were mixed with precoated latex beads ($2 \times 10^5$), incubated for 30 min at 37°C in Hanks balanced salt solution (HBSS)–2% bovine serum albumin (BSA), and plated on FN-coated slides. Slides were fixed and immunostained for tubulin. Redistribution of mitochondria and MTOC was considered to have occurred if they were more abundant in the third of the cell centered on the contact with the latex bead.

**Immunoblotting and coimmunoprecipitation.** After the indicated treatment, CEM and CH7C17 T cells were lysed as described previously (12). For coimmunoprecipitation assays, transfected HEK293T cells or primary T lymphoblasts were lysed in ice-cold lysis buffer containing 0.5% Triton X-100 as described previously (14). Lysates were centrifuged at 16,000 × $g$ for 10 min at 4°C, and the resulting supernatants were precleared for 1 h at 4°C with protein G Dynabeads (Life Technologies) and incubated for 3 h with anti-GFP or with anti-Miro-1. Immunocomplexes were collected by incubation with protein G Dynabeads for 1 h. The samples were thereafter washed six times with ice-cold lysis buffer and processed for Western blotting. Proteins were separated by SDS-PAGE and visualized with Fujifilm LAS-3000 after membrane incubation with specific primary antibodies and peroxidase-conjugated secondary antibodies. Band intensities were quantified using Image Gauge software (Fujifilm) and results normalized to α-tubulin or, for phosphoproteins, to total protein expression.

**Parallel-plate flow chamber analysis of endothelial cell-leukocyte interactions and detachment.** PBLs, T lymphoblasts, peripheral blood mononuclear cells (PBMCs), and CEM cells ($1 \times 10^6$/ml) were drawn across activated confluent HUVEC monolayers at an estimated shear stress of 1.8 dynes (dyn)/cm$^2$ (assumed as physiological for human post-capillary venules where transmigration takes place) for the required time. The shear stress was applied as described previously (23).

Control and Miro-1-silenced CEM cells were first labeled with DiO, Dil, or Did and then with Mitotracker Orange or Green. Cells ($10^6$/ml from each type) were drawn across on activated confluent HUVEC monolayers with a shear stress of 1.8 dyn/cm$^2$. Images were acquired every 30 s. Cells labeled with different cell trackers or Mitotrackers displayed similar results, confirming that there was no interference with the cellular processes analyzed.

For detachment experiments, control and Miro-1-silenced CEM cells were preincubated with Mitotracker Orange or Green to distinguish them and allowed to adhere for 5 min at 37°C to activated HUVEC monolayers. Shear stress was started at 0.5 dyn/cm$^2$ and increased up to 15 dyn/cm$^2$. Cell detachment was calculated by normalizing the number of adhered cells to the number observed at the flow rate of 0.5 dyn/cm$^2$.

**Adhesion assays.** HUVEC were grown to confluence in 96-microwell plates (Costar) and activated with TNF-α. CEM or CH7C17 cells were labeled with 1 μM BCECF-AM and adhered to the activated HUVEC (21). In other experiments, CEM cells ($1 \times 10^6$/ml) were left untreated or pretreated with 4 μM oligomycin or 10 μM Ru360 (30 min) and washed and resuspended in HBSS–2% FCS. The cells were then adhered to activated HUVEC in 6-well plates for 30 min at 37°C under static conditions or with continuous rotation (60 rpm). After incubation, the plates were washed three times with HBSS, and adhered cells were fixed with 4% PFA. The effects of inhibitors on lymphocyte adhesion were assessed by counting the number of adhered cells using the CellCounter ImageJ plug-in. Results were normalized to those for untreated cells adhered to activated HUVEC. Cells adhered to nonactivated HUVEC were used as a negative control.

**Migration and transmigration assays.** Migration assays were performed in 5-μm-pore-size Transwell cell culture chambers (Costar) (30). Transmigration through a confluent monolayer of activated HUVEC was assayed in 5-μm-pore-size Transwell plates (23). The number of migrated cells was measured by flow cytometry.

**3D migration assay.** Migration of CEM T cells through a 3D collagen matrix was assayed according to the manufacturer's instructions (Ibidi). Control and Miro-1-silenced CEM cells were preincubated with DiD or Dil, and images were acquired every 5 min for standard assays (see Fig. 4C) and every 3 min for titration experiments (see Fig. 4D). Images were analyzed using the Manualtracking and Chemotaxis Tool ImageJ plug-ins.

**F-actin determination.** Levels of polymerized actin were measured as described previously (31). Briefly, cells ($1 \times 10^5$ per well of a 96-well plate) were incubated with 10 nM CXCL12 at 37°C for the indicated times. Cells were then fixed, permeabilized, and stained with phalloidin-Alexa Fluor 647 (Invitrogen). Fluorescence intensity was determined in a FACSCanto flow cytometer (BD Biosciences) and analyzed with Flow-Jo software.

Results are expressed as the fold increase in mean fluorescence intensity relative to that of the cells not exposed to CXCL12.

**Flow cytometry calcium measurement.** To track intracellular calcium levels in cells in suspension, control and Miro-1-silenced CEM cells were incubated with DiD or Dil and Fluo4-AM, and after 1 min of baseline recording, CXCL12 was added (10 nM). Calcium flux was measured over time using a FACSCanto flow cytometer. Ionomycin (0.5 mg/ml) was used as a positive control. Data were analyzed with Flow-Jo software.

**ATP measurement.** For intracellular ATP quantifications, frozen cells were homogenized with a lysis buffer (25 mM Tris-HCl [pH 7.5], 0.1% Triton X-100), and ATP was rapidly measured by a coupled luciferin-luciferase reaction (32) with an ATP determination kit (Invitrogen, Paisley, United Kingdom). For protein quantification, a colorimetric method (Pierce bicinchoninic acid [BCA] protein assay kit) was used following the manufacturer's instructions.

**Mitochondrial membrane potential.** The mitochondrion-directed fluorescence-sensitive probe JC-1 was used to determine variations in mitochondrial membrane potential ($\Delta\psi_m$) (12). Briefly, CEM T cells ($1 \times 10^5$ per well of a 96-well plate) were preloaded with JC-1 (2 mg/ml) and stimulated with 10 nM CXCL12 at 37°C for the indicated times. FL1 (520 nm) and FL2 (590 nm) emissions were recorded in a FACSCanto flow cytometer and analyzed with Flow-Jo software.

**Statistical analysis.** Statistical analysis and comparisons were made with GraphPad Prism5. Data were tested for normality using the D'Agostino-Pearson omnibus normality test or using the Kolmogorov-Smirnov test when the sample was small due to experimental conditions. Differences between means were tested by Student's *t* test for normal data. Data were analyzed using one-way analysis of variance (ANOVA) with the Bonferroni posttest (for Fig. 2D and 5D and for Fig. S4A in the supplemental material) and with the Tukey posttest (for Fig. 7D) or using two-way ANOVA with the Bonferroni posttest (for Fig. 3D).

## RESULTS

**Mitochondrial positioning to the adhesion zone during leukocyte-endothelial cell interaction.** We first assessed the specific redistribution of leukocyte mitochondria during the interaction between leukocyte and endothelial cells. Using time-lapse confocal microscopy, we tracked lymphocyte mitochondria, using mitochondrion-targeted fluorescent proteins or with Mitotracker Orange, during their interaction with TNF-α-activated primary human umbilical vein endothelial cells (HUVEC). During static adhesion of human T lymphoblasts to activated HUVEC, most lymphocyte mitochondria localized to the leukocyte-HUVEC contact zone. During subsequent polarization of the migrating lymphoblast, we observed a further relocalization of mitochondria toward the uropod (Fig. 1A; see Movie S1 in the supplemental material). The initial redistribution of mitochondria to the contact zone during endothelial adhesion was also observed in the T-cell line CEM under both static and flow conditions (Fig. 1B). This biphasic mitochondrial repositioning, with initial concentration at the endothelial contact zone followed by polarization to the uropod in migrating cells, was also seen under physiological flow conditions and with freshly isolated leukocyte populations (see Fig. S1A and B in the supplemental material). These data indicate that redistribution of mitochondria to the adhesion zone and later to the uropod constitutes a cellular signature of the attachment of leukocytes to endothelium and their subsequent migration.

Mitochondria bind microtubule-associated proteins (MAPs) and move along the microtubule network (6). To monitor the redistribution of the microtubule-organizing center (MTOC) and mitochondria in lymphocytes adhering to activated endothelium (Fig. 1C), we transfected human T lymphoblasts with paxillin-GFP (33) and mtRFP to simultaneously track the MTOC and mitochondria (Fig. 1D). During lymphocyte adhesion, most lymphocyte mitochondria and the MTOC moved in a concerted fashion to the contact zone with the endothelium (Fig. 1D). In the reverse experiment, in which endothelial mitochondria were tracked by labeling with mtYFP, we did not detect a significant shift of position upon lymphocyte adhesion (Fig. 1E). Confocal microscopy revealed that endothelial mitochondria colocalized with tubulin but not with the actin cytoskeleton (see Fig. S1C in the supplemental material). In addition, endothelial mitochondria were not present at the docking structure (23) formed after leukocyte arrest on the endothelium (see Fig. S1D in the supplemental material). These results indicate that mitochondrial redistribution is a specific process in leukocytes during interaction with endothelium.

**Mitochondrial redistribution depends on lymphocyte integrin engagement.** We next assessed whether mitochondrial relocalization to the contact zone with endothelium is dependent on specific interactions between lymphocyte integrins and adhesion molecules present on activated endothelium. For this, we added lymphoblasts to resting or TNF-α-activated HUVEC and quantified mitochondrial density as the percentage of the total mitochondrial fluorescence intensity located in the contact area (the third of the cell adjacent to the contact site) (Fig. 2A). Upon adhesion to activated endothelial cells, about 60% of mitochondrial fluorescence was present at the contact area, contrasting with 30% upon adhesion to nonactivated endothelium (Fig. 2A). To dissect the role of lymphocyte integrins, we incubated T lymphocytes with beads coated with ICAM-1 or VCAM-1, the ligands of integrins LFA-1 and VLA-4, respectively, or with BSA as a negative control (Fig. 2B). Engagement of VLA-4 or LFA-1 by their specific ligands significantly increased translocation of both mitochondria and MTOC. The translocation rates of both MTOC and mitochondria in response to VLA-4 engagement (with fold inductions in comparison to BSA of 2.1 for MTOC and 1.65 for mitochondria) were higher than those observed with LFA-1 (1.5 and 1.25, respectively) (Fig. 2B and C). Furthermore, T lymphoblasts treated with specific LFA-1 or VLA-4 inhibitors and added to TNF-α-activated HUVEC showed a clear reduction in mitochondrial translocation in comparison to the untreated cells (Fig. 2D), as assessed by mitochondrial fluorescence intensity localized at the contact area with endothelium. These data demonstrate that specific engagement of both VLA-4 and LFA-1 is sufficient to promote MTOC and mitochondrial translocation toward the cell-to-cell contact during lymphocyte adhesion to endothelium.

Retrograde movement of mitochondria along microtubules (toward the minus end, where MTOC is allocated) is mediated by dynein (6). Cytoplasmic dynein is a multisubunit microtubule motor complex that, together with its activator dynactin, drives vesicular cargo toward the minus ends of microtubules (34). Specific silencing of dynein heavy chain (DHC) in T lymphocytes (see Fig. S2A in the supplemental material) uncoupled mitochondria from the MTOC and impaired the recruitment of both organelles to the contact zone (see Fig. S2B in the supplemental material). These cells showed an impaired ability to adhere to activated HUVEC (see Fig. S2C in the supplemental material).

**Miro-1 regulates mitochondrial redistribution and firm lymphocyte adhesion to activated endothelium.** Miro-1 is a calcium-dependent sensor that controls mitochondrial motility along microtubules and therefore mitochondrial trafficking (14–17). We examined the possible involvement of Miro-1 in mito-

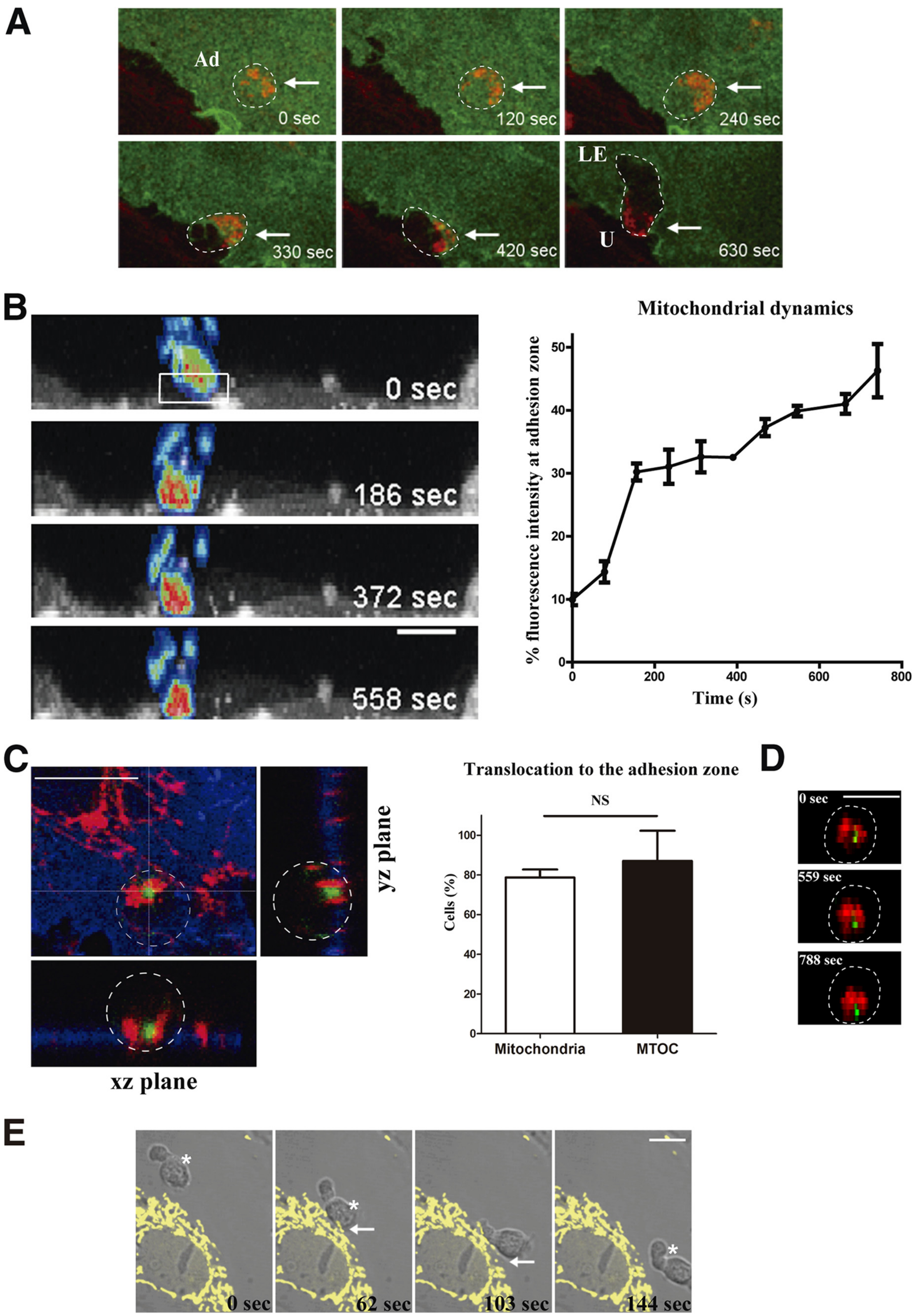
A
Ad
0 sec
120 sec
240 sec
330 sec
420 sec
LE
U
630 sec
B
0 sec
186 sec
372 sec
558 sec
Mitochondrial dynamics
% fluorescence intensity at adhesion zone
0
10
20
30
40
50
Time (s)
0
200
400
600
800
C
yz plane
xz plane
Translocation to the adhesion zone
NS
Cells (%)
0
20
40
60
80
100
Mitochondria
MTOC
D
0 sec
559 sec
788 sec
E
*
0 sec
62 sec
103 sec
144 sec

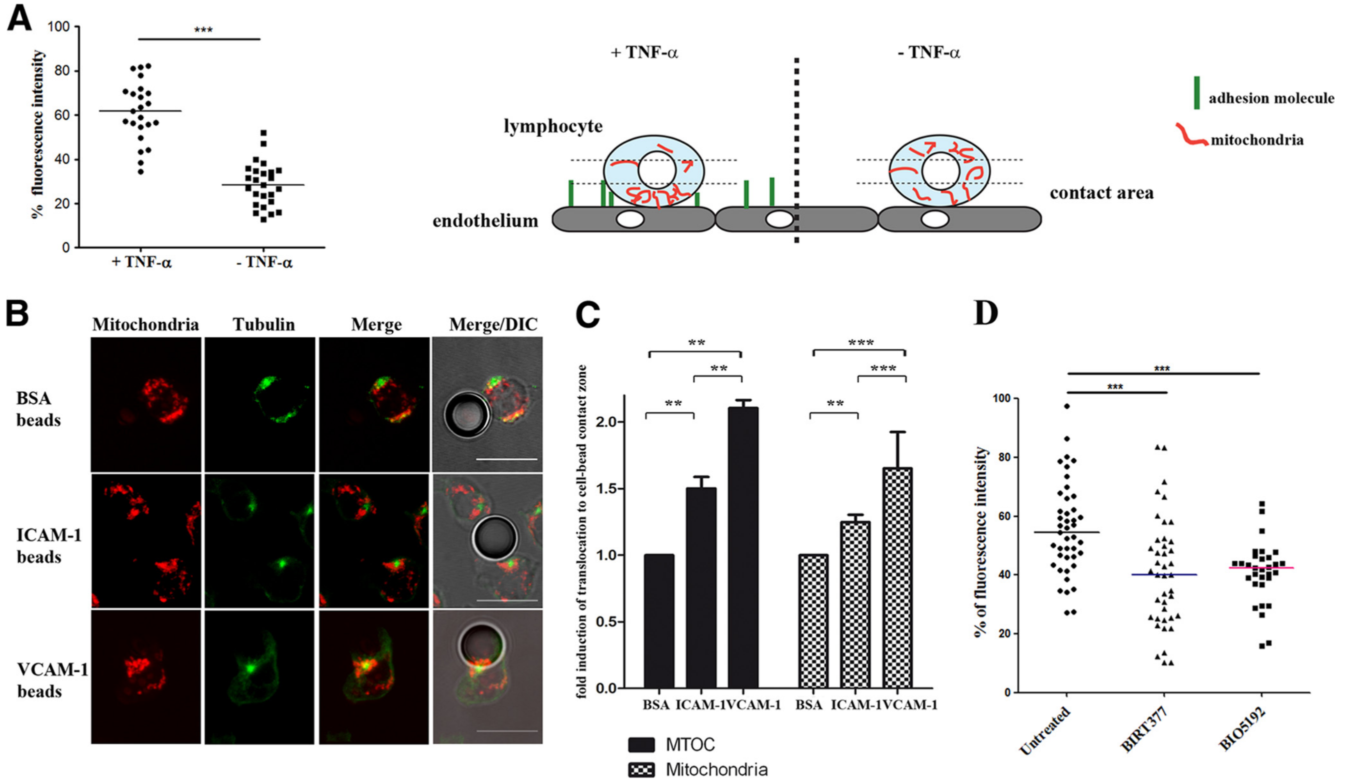

**FIG 2** Mitochondrial redistribution depends on integrin engagement. (A) Quantification of mitochondrial redistribution in lymphoblasts adhered to resting or activated HUVEC monolayers. Mitochondrial redistribution is calculated as the percentage of mitochondrial fluorescence intensity (maximal Z-stack projections of Mitotracker Orange staining) located in the contact area with endothelial cells (defined as the third of the cell close to the HUVEC monolayer; see scheme). Data are shown as a scatter plot; horizontal lines depict medians of 23 and 25 unpolarized cells adhered, respectively, on either TNF-α-activated or nonactivated HUVEC. Three independent experiments were performed (***, $P < 0.001$). The scheme illustrates the method used to quantify mitochondrial redistribution. (B) Representative images of conjugates formed between CH7C17 cells and latex beads coated with BSA, ICAM-1, or VCAM-1, stained for α-tubulin (green) and mitochondria (red). DIC, differential interference contrast. Scale bars, 10 μm. (C) Fold inductions, in comparison to a BSA negative control, of MTOC and mitochondrial relocalization toward the coated beads. A minimum of 30 (BSA), 95 (VCAM-1), or 140 (ICAM-1) cells were analyzed for each experiment. (D) Quantification of mitochondrial redistribution in lymphoblasts untreated ($n = 43$) and pretreated (15 min at 37°C) with BIRT377 ($n = 41$) or BIO5192 ($n = 31$) to block LFA-1 or VLA-4 integrins and incubated with activated TNF-α-activated HUVEC for 20 min. Data are shown as a scatter plot; horizontal lines depict medians from two independent experiments of nonpolarized cells adhered to activated HUVEC (***, $P < 0.001$; **, $P < 0.01$ [by one-way ANOVA]).

chondrial translocation during lymphocyte adhesion. Depletion of Miro-1 with a specific siRNA (Fig. 3A), which did not affect Miro-2 expression (see Fig. S3A in the supplemental material), decreased mitochondrial translocation in T cells adhered to activated HUVEC (Fig. 3B), suggesting that Miro-1 controls mitochondrial positioning in response to integrin engagement in T cells. In contrast to DHC-silenced cells (see Fig. S2C), Miro-1-depleted ones showed a slight but nonsignificant decrease of cell adhesion under static conditions (Fig. 3C). A critical step during lymphocyte interaction with the endothelium is firm adhesion. Therefore, we analyzed the role of Miro-1 in firm adhesion by measuring the resistance of T lymphocytes to be detached from endothelium under increasing shear stress. Importantly, Miro-1-silenced T cells detached more readily than controls from HUVEC

---

**FIG 1** Mitochondrial dynamics during leukocyte-endothelium interaction. (A) Representative images from a time-lapse video microscopy analysis of human T lymphoblasts loaded with Mitotracker Orange (red) and adhered to a TNF-α-activated HUVEC monolayer transfected with ICAM-1–GFP (green). Maximal projections of stacks near the endothelial monolayer are shown; dashed lines delineate cell contours of adhering lymphocytes, and arrows mark sites of leukocyte mitochondrial accumulation. Ad, adhered lymphocyte; LE, lymphocyte leading edge; U, lymphocyte uropod. (B) Time-lapse sequence of orthogonal maximal projections of CEM T cells transfected with mtRFP (fluorescence intensity color gradient) adhering to an activated HUVEC monolayer transfected with ICAM-1–YFP (gray scale). The graph shows the percentage of T-cell mitochondrial fluorescence intensity at the contact area (illustrated in the boxed region at time zero, representing a third of the cell close to the HUVEC monolayer) during the adhesion, under flow conditions (1.8 dyn/cm$^2$), of CEM cells. (C) Left panel, representative horizontal and orthogonal sections of a lymphoblast adhered to an activated HUVEC monolayer. Cells were stained with anti-MnSOD (red), anti-ICAM-1 (blue), and antitubulin-FITC (green). Right panel, histograms showing translocation of mitochondria and MTOC toward the contact zone in human lymphoblasts adhered to activated HUVEC monolayers. Data are means ± standard deviation (SD) from two independent experiments ($n = 205$ cells). NS, nonsignificant difference. (D) Representative orthogonal maximal projections from a time-lapse sequence of a human T lymphoblast transfected with paxillin-GFP (green) and mtRFP (red) adhering to an activated HUVEC monolayer (not shown); dashed lines delineate the cell contour of the adhering lymphocyte. (E) Time-lapse sequence of a human PBL (asterisk) migrating toward an activated HUVEC monolayer transfected with mtYFP (yellow). Arrows mark the endothelial area in contact with the PBL. Scale bars, 10 μm.

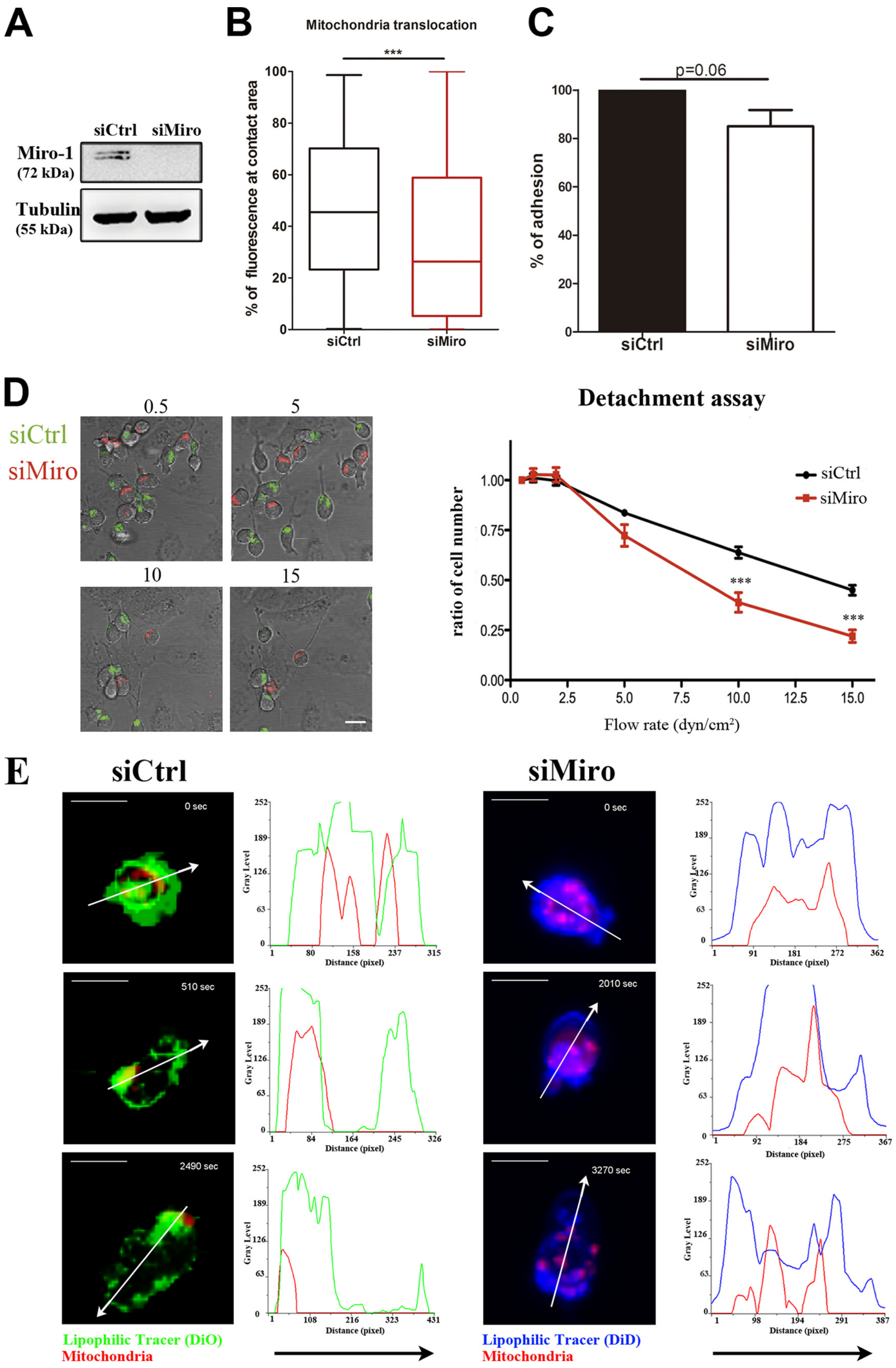
A
siCtrl
siMiro
Miro-1
(72 kDa)
Tubulin
(55 kDa)
B
Mitochondria translocation
***
% of fluorescence at contact area
0
20
40
60
80
100
siCtrl
siMiro
C
p=0.06
% of adhesion
0
20
40
60
80
100
siCtrl
siMiro
D
siCtrl
siMiro
0.5
5
10
15
Detachment assay
ratio of cell number
0.00
0.25
0.50
0.75
1.00
siCtrl
siMiro
***
***
0.0
2.5
5.0
7.5
10.0
12.5
15.0
Flow rate (dyn/cm²)
E
siCtrl
0 sec
510 sec
2490 sec
Gray Level
Distance (pixel)
0
63
126
189
252
1
80
158
237
315
1
84
164
245
326
1
108
216
323
431
Lipophilic Tracer (DiO)
Mitochondria
siMiro
0 sec
2010 sec
3270 sec
1
91
181
272
362
1
92
184
275
367
1
98
194
291
387
Lipophilic Tracer (DiD)
Mitochondria

at a flow rate of 5 dyn/cm$^2$ or above (Fig. 3D), suggesting a specific role of Miro-1 in regulating the strength of lymphocyte adhesiveness. To explore the role of Miro-1 in lymphocyte polarization, we analyzed the shape of lymphocytes during adhesion to HUVEC under flow conditions by measuring their elliptical form factor. Interestingly, under these conditions, hyperpolarized cells were present in control but not Miro-1-silenced cells (see Fig. S3 in the supplemental material). We next investigated whether the defects observed under physiological flow conditions both in firm adhesion and polarization were accompanied by impaired mitochondrial dynamics. Miro-1-depleted cells presented an evident impaired ability to firmly adhere, polarize, and migrate (see Movie S2 in the supplemental material). Moreover, mitochondrial redistribution to the uropod during polarization and the subsequent migration were greatly affected (Fig. 3E; see Movie S3 in the supplemental material).

**Miro-1 knockdown impairs lymphocyte chemotaxis.** To assess whether Miro-1 regulates lymphocyte migration capability, we examined CXCL12-induced migration of control and Miro-1-silenced cells in modified Boyden chemotaxis chambers coated with a TNF-α-activated HUVEC monolayer or uncoated. In both cases, Miro-1-silenced cells migrated less efficiently along the chemotactic gradient (Fig. 4A and B). Miro-1 knockdown also disrupted the directionality and reduced the speed of T-cell migration toward CXCL12 in 3D collagen gels (Fig. 4C). These data indicate that expression of Miro-1 is essential for proper directional lymphocyte migration in response to a chemotactic stimulus not only under conditions greatly dependent on integrin function but also in an integrin-independent migration mode (35). We further analyzed the contribution of Miro-1 during lymphocyte migration within 3D gels containing different collagen concentrations. Remarkably, Miro-1-silenced cells migrate slower than control cells through different collagen densities (Fig. 4D). It is noteworthy that both control and Miro-1-depleted cells showed the same trend in the decrease of mean velocity at increasing collagen densities (35).

**Miro-1 controls CXCL12-mediated lymphocyte polarization and mitochondrion-MTOC association.** Chemokines can increase lymphocyte adhesion to endothelium and also induce the acquisition of a polarized, promigratory cell shape (36). CXCL12-induced polarization was impaired in Miro-1-silenced cells (Fig. 5A).

Upon Ca$^{2+}$ binding to its EF-hands, Miro-1 undergoes a conformational change resulting in the dissociation of mitochondria from microtubule track (19). Therefore, we studied polarization after CXCL12 stimulation in lymphocytes overexpressing GFP (as a negative control), GFP-Miro, or GFP-Miro$^{KK}$, a Miro-1 form with the double mutation E208K E328K that is incapable of Ca$^{2+}$ binding in its EF motifs (14). The overexpression of Miro-1$^{KK}$ with EF motif mutations was able to decrease CXCL12-induced polarization (Fig. 5B; see Movie S4 in the supplemental material). Moreover, we assessed the effect on CXCL12-mediated polarization of Miro-1$^{KK}$ overexpression in cells previously silenced for Miro-1. As shown in Fig. S4A in the supplemental material, the overexpression of GFP-Miro1$^{KK}$ did not restore cell polarity whereas GFP-Miro1 rescued the phenotype observed in control cells, underlining the importance of Miro-1 calcium binding domains for its correct function in chemokine-induced lymphocyte polarity.

We next assessed whether the defect in adhesion strength of Miro-1-silenced cells as well as in polarization of both Miro-1-silenced and Miro$^{KK}$-expressing cells might be related to impaired association of mitochondria with the MTOC. For this, we plated T cells on a fibronectin (FN) or poly-L-lysine (PLL) matrix containing CXCL12 and measured the distance between the center of mass of mitochondrial fluorescence and the MTOC. In control cells, CXCL12 stimulation reduced the distance between mitochondria and the MTOC at the uropod (Fig. 5C and D; see Movie S5 in the supplemental material). This effect of CXCL12 was not observed in Miro-1-silenced cells (Fig. 5C and D; see Fig. S4B and Movie S5 in the supplemental material), supporting the importance of Miro-1 in the relocalization of the MTOC and mitochondria to the uropod. Moreover, T cells overexpressing GFP-Miro$^{KK}$ showed a reduced proximity of MTOC and mitochondria induced by CXCL12 in comparison with T cells overexpressing GFP-Miro (Fig. 5E and F; see Fig. S4C and Movie S6 in the supplemental material). Upon chemokine stimulation, mitochondria first redistribute toward the uropod (9) together with the MTOC. Our results indicate that Ca$^{2+}$ binding to Miro-1 EF-hands might lead to a conformational change in Miro-1, resulting in the halt of mitochondria in this specific subcellular location.

The effect of targeting Miro-1 by either silencing or GFP-Miro$^{KK}$ was exerted specifically at the mitochondrion/MTOC polarized association, since other cell polarity parameters such as membrane receptors or cytoskeletal proteins (ICAM-3 or ERM) remained unaltered (see Fig. S4B and C in the supplemental material).

To rule out possible pleiotropic effects produced by Miro-1 knockdown on the microtubular skeleton, we have assessed parameters such as the general conformation and dynamics of the tubulin network and the localization of the Golgi apparatus (GA) (37). Neither the tubulin network nor the GA was apparently altered. Hence, the GA showed its usual localization around the MTOC in both control and silenced cells (see Fig. S5A in the

**FIG 3** Miro-1 regulates mitochondrial redistribution during adhesion and migration on endothelium. (A) Western blot analysis of siRNA Miro-1 silencing in CEM T cells. (B) Box and whiskers plot (minimum to maximum) of mitochondrial redistribution in control and Miro-1-silenced cells adhered to TNF-α-activated HUVEC monolayers. Mitochondrial redistribution is calculated as the percentage of mitochondrial fluorescence intensity located at the contact area (defined as the third of the cell close to the HUVEC monolayer). Data are medians ± interquartile ranges for 247 (siCtrl) and 291 (siMiro-1) cells from three independent experiments (***, $P < 0.001$). (C) Quantification of lymphocyte adhesion on a TNF-α-activated HUVEC monolayer in control and Miro-1-silenced cells. Data are means ± standard errors of the means (SEM) from three independent experiments. (D) Representative images of control CEM T cells (siCtrl; Mitotracker Green) and Miro-1-silenced cells (siMiro; Mitotracker Orange) adhered to activated HUVEC under increasing shear stress (flow rate from 0.5 to 15 dyn/cm$^2$). The right panel shows adhered cells at different flow rates as a proportion of adherence at 0.5 dyn/cm$^2$. Data are from a representative experiment and are the means ± SEM for nine fields; **,*$P < 0.001$ (by two-way ANOVA). (E) Representative images from time-lapse video microscopy of control and Miro-1-silenced cells prestained with Mitotracker Orange and with DiO (siCtrl; green) and DiD (siMiro; blue) adhering and migrating on TNF-α-activated HUVEC pretreated with CXCL12 (1 μM) under physiological laminar flow conditions (1.8 dyn/cm$^2$). The right part of each image shows the fluorescence intensity distribution (gray values) across the cells (depicted by arrows). Scale bars, 10 μm.

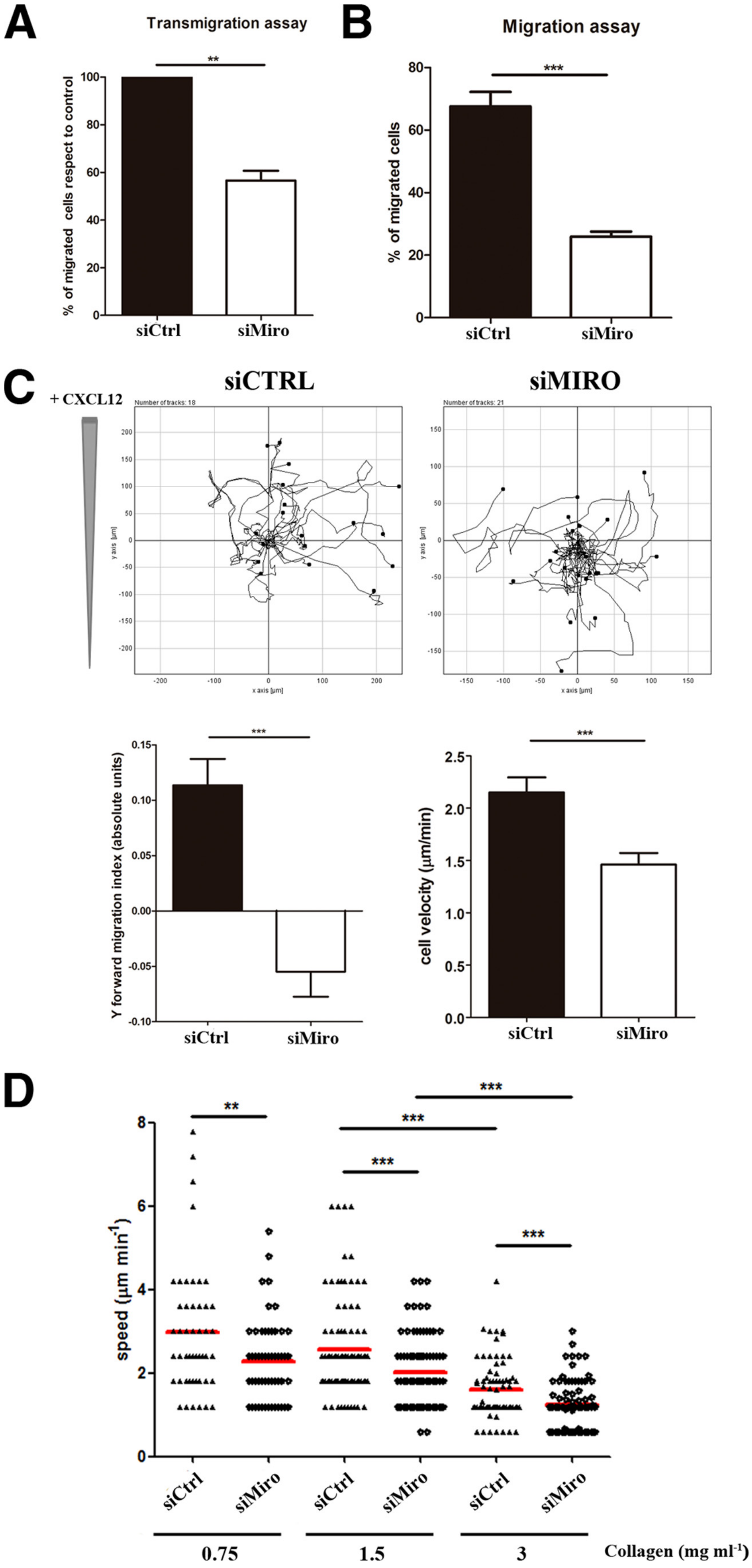
A
Transmigration assay
**
% of migrated cells respect to control
0
20
40
60
80
100
siCtrl
siMiro
B
Migration assay
***
% of migrated cells
0
20
40
60
80
siCtrl
siMiro
C
+ CXCL12
siCTRL
siMIRO
Number of tracks: 18
Number of tracks: 21
y axis [µm]
x axis [µm]
Y forward migration index (absolute units)
***
0.15
0.10
0.05
0.00
-0.05
-0.10
siCtrl
siMiro
cell velocity (µm/min)
***
2.5
2.0
1.5
1.0
0.5
0.0
siCtrl
siMiro
D
speed (µm min$^{-1}$)
**
***
***
***
***
0
2
4
6
8
siCtrl
siMiro
siCtrl
siMiro
siCtrl
siMiro
0.75
1.5
3
Collagen (mg ml$^{-1}$)

supplemental material). Moreover, the analysis of microtubule dynamics in control and Miro-1-silenced cells showed similar microtubule growth rates (siCtrl, 14.60 ± 3.11 $\mu m \cdot min^{-1}$; siMiro, 15.01 ± 2.82 $\mu m \cdot min^{-1}$) (see Fig. S5B and Movie S7 in the supplemental material). Furthermore, membrane expression of several cell markers, including integrins and the CXCL12 receptor CXCR4, as well as the CXCL12-mediated endocytosis of CXCR4, was largely unaffected (see Fig. S5C and D in the supplemental material).

These results indicate that Miro-1 mediates mitochondrial positioning and MTOC association, a phenomenon specifically implicated in the chemokine-induced acquisition of a polarized morphology by lymphocytes.

**Miro-1 associates with the dynein complex and contributes to regulate CXCL12-induced lymphocyte activation.** To investigate how Miro-1 controls mitochondrial positioning, we transfected HEK293T cells with GFP-Miro-1 or GFP alone and examined GFP immunoprecipitates from these cells. The dynein p74 intermediate chain and the dynactin p50 subunit were specifically detected in GFP–Miro-1 immunoprecipitates (Fig. 6A). Therefore, we analyzed this interaction in endogenous complexes from human T lymphoblast lysates. Dynein heavy chain and the $p150^{glued}$ component of dynactin were coimmunoprecipitated with Miro-1 in these cells (Fig. 6A, right panel). Hence, Miro-1 appears to be a specific mediator of the interaction between mitochondria and the dynein/dynactin motor complex.

To explore the molecular basis of inhibited polarization in Miro-1-silenced T cells, we studied molecular hallmarks of chemokine-induced lymphocyte polarization. One of these hallmarks is rapid actin polymerization (38), and we detected decreased actin polymerization in response to CXCL12 in Miro-1-silenced cells (Fig. 6B and C). Another polarity hallmark in T cells is myosin light-chain (MLC) phosphorylation, which is required for efficient retraction of the uropod by myosin II (30). Interestingly, CXCL12-induced MLC phosphorylation was inhibited in the uropods of Miro-1-silenced cells (Fig. 6D), suggesting a specific role of Miro-1 in cell polarization.

We next examined the intracellular calcium dynamics in response to CXCL12 stimulation and during lymphocyte migration on activated endothelium. Interestingly, when cells were stimulated with CXCL12 in suspension, we observed no significant differences between control and Miro-1-silenced cells (Fig. 7A). In contrast, when T cells adhered and migrated on activated endothelium, Miro-1 depletion had a negative impact on the intensity and duration of calcium peaks (Fig. 7B and C). These data indicate that Miro-1 regulates intracellular calcium not on a general scale but in a subcellular context.

Mitochondrial activity is reflected in the electrical potential ($\Delta\psi_m$) across the inner membrane and has a direct influence on axonal transport (39). It has been shown that an increased $\Delta\psi_m$ enhances the rate of mitochondrial transport, most obviously retrograde movement (40). We found that CXCL12 increased $\Delta\psi_m$, but no significant differences were observed between the responses of control and Miro-1-silenced T cells (see Fig. S6 in the supplemental material). Miro-1 depletion thus appears to affect CXCL12-induced movement of mitochondria without significantly affecting their intrinsic activation capacity. Moreover, to rule out possible alterations in mitochondrial functioning due to the downmodulation of Miro-1 expression, we assessed ATP cellular content in both control and Miro-1-silenced cells. Control and Miro-1-silenced cells had similar ATP contents, and CXCL12 stimulation led to a significant reduction in ATP levels in both (Fig. 7D).

Chemokine receptors activate multiple signaling pathways, leading to varied functional outcomes, including adhesion, polarization, and chemotaxis (41). Among these, the ERK1/2 phosphorylation is one of most characterized cell signaling signatures (42). Therefore, we assessed the role of Miro-1 in the modulation of signaling downstream of the CXCL12 receptor through the study of the phosphorylation kinetics of ERK1/2. Maximal ERK1/2 phosphorylation was detected within 2 min of chemokine stimulation in control T cells, and this effect was clearly inhibited in Miro-1-silenced cells (Fig. 7E).

## DISCUSSION

In this study, we demonstrate that mitochondria relocalize to the contact area during lymphocyte adhesion to endothelial monolayers and that this is directed by the GTPase Miro-1. Redistribution of mitochondria is specific to leukocytes and is not observed in endothelial cells. The movement of mitochondria involves the LFA-1/ICAM-1 and VLA-4/VCAM-1 receptor/counterreceptor pairs.

It has been reported that the MTOC and mitochondria can be recruited by chemokine-activated LFA-1 at the immunological synapse (43). Here, we provide evidence that the signal generated by VLA-4 is even more efficient in the redistribution of both MTOC and mitochondria. In our model, mitochondrial arrest in the cellular zone of integrin engagement might be related to local actin polymerization and increased intracellular $Ca^{2+}$. The cytoplasmic tail of the α4 subunit of VLA-4 interacts with paxillin (44), which is a docking protein for other cytoskeletal proteins such as F-actin, for tyrosine kinases, and for GTPase-activating proteins (45). Moreover, VLA-4 engagement can promote the tyrosine phosphorylation of a broad range of proteins, including proline-rich tyrosine kinase 2 (Pyk2), focal adhesion kinase (FAK), and c-Src (46), resulting in the activation of several pathways. Accordingly, increased intracellular $Ca^{2+}$ and LFA-1 engagement triggers activation and redistribution of Pyk2 to the MTOC in T lymphoblasts (47). All these signaling cascades might

**FIG 4** Miro-1 controls lymphocyte migration and chemotaxis. (A) Quantification of the transmigration of control and Miro-1-silenced CEM T cells across Transwell filters (5-μm pore size) coated with a TNF-α-activated HUVEC monolayer (see Materials and Methods). Data are expressed as a percentage with respect to transmigrated control cells. (B) Migration of control and Miro-1-silenced CEM T cells across uncoated Transwell filters. Migration is calculated as a percentage of input cells. Data in panels A and B are means ± SEM for two independent experiments run by duplicate (***, $P < 0.001$; **, $P < 0.01$). (C) Cell trajectory plots of control and Miro-1-silenced cells migrating toward CXCL12 in a collagen matrix (1.6 mg $ml^{-1}$). The upper panels show results from a representative experiment out of three. The lower panels show quantification of movement toward the chemokine (Y forward migration index) and cell speed ($\mu m\ min^{-1}$) of 98 control and 102 Miro-1-silenced cells from three independent experiments (mean ± SEM; ***, $P < 0.001$). (D) Velocities of single migrating control and Miro-1-silenced CEM cells (dots) in collagen gels with various densities. Data are shown as a scatter plot; horizontal lines depict means from three independent experiments (***, $P < 0.001$; **, $P < 0.\ 01$).

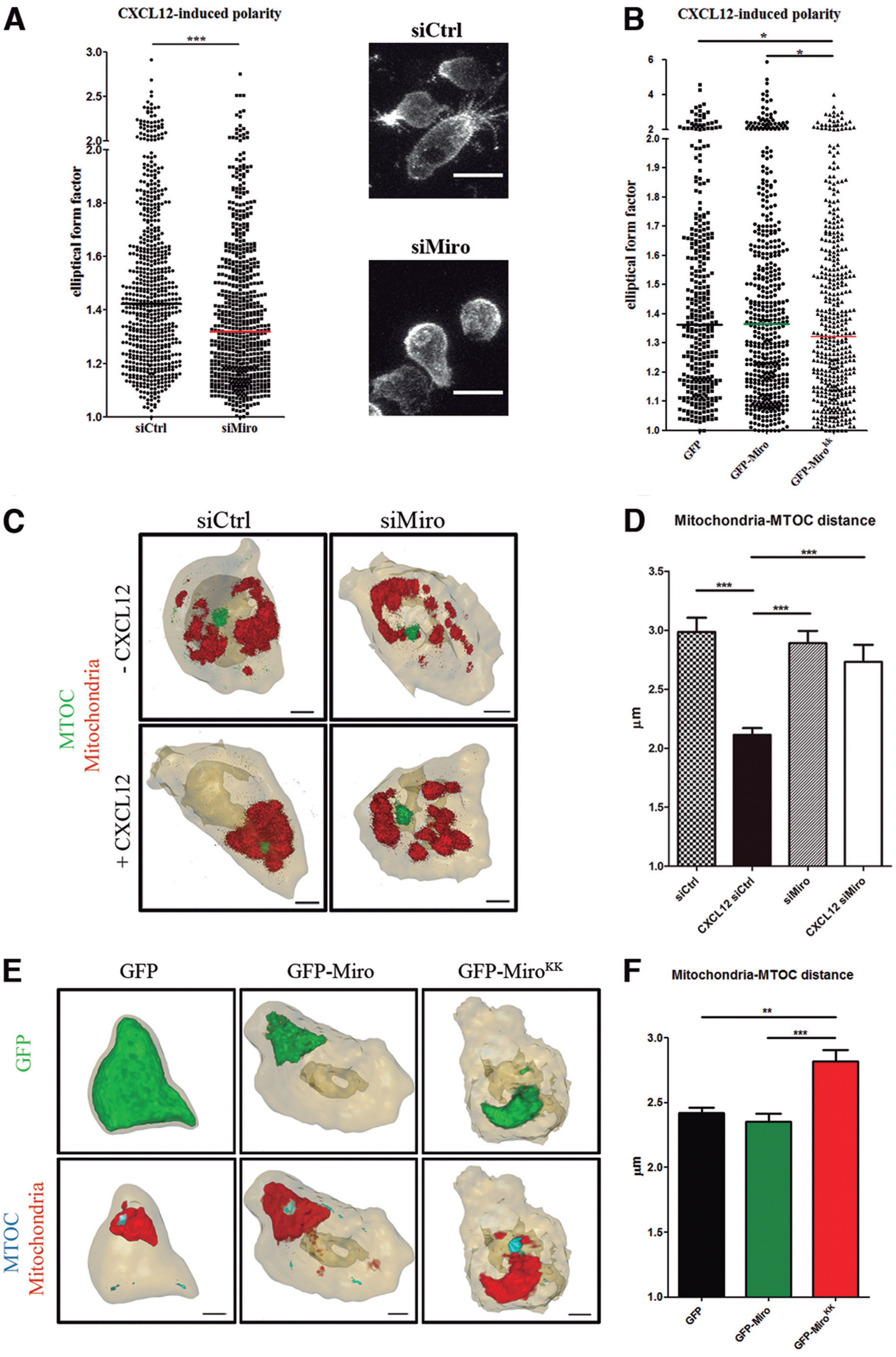
A
CXCL12-induced polarity
***
3.0
2.5
2.0
1.8
1.6
1.4
1.2
1.0
elliptical form factor
siCtrl
siMiro
siCtrl
siMiro
B
CXCL12-induced polarity
*
*
6
4
2
2.0
1.9
1.8
1.7
1.6
1.5
1.4
1.3
1.2
1.1
1.0
elliptical form factor
GFP
GFP-Miro
GFP-Miro$^{KK}$
C
siCtrl
siMiro
- CXCL12
+ CXCL12
MTOC
Mitochondria
D
Mitochondria-MTOC distance
***
***
***
3.5
3.0
2.5
2.0
1.5
1.0
µm
siCtrl
CXCL12 siCtrl
siMiro
CXCL12 siMiro
E
GFP
GFP-Miro
GFP-Miro$^{KK}$
GFP
MTOC
Mitochondria
F
Mitochondria-MTOC distance
**
***
3.0
2.5
2.0
1.5
1.0
µm
GFP
GFP-Miro
GFP-Miro$^{KK}$

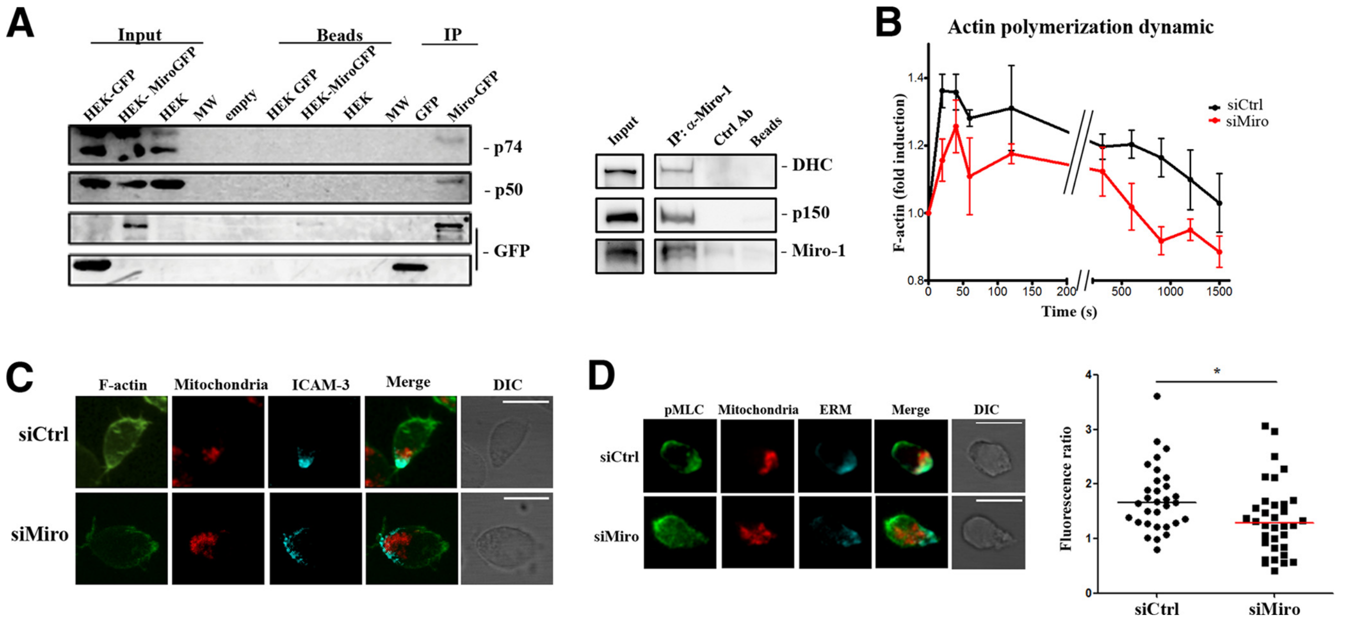

**FIG 6** Miro-1 connects mitochondria to the microtubule retrograde transport machinery and regulates CXCL12-induced cytoskeleton activation. (A) Coimmunoprecipitation analysis showing association of Miro-1 with the dynein motor complex. Complexes (IP) were precipitated from cell lysates of transfected HEK293 cells (input) with anti-GFP and probed with anti-p74, anti-p50, and anti-GFP (left panel) or from human primary T lymphoblasts with anti-Miro-1 antibody and probed with anti-dynein heavy chain (DHC), anti-p150, and anti-Miro-1 (right panel). (B) Actin polymerization dynamics in control or Miro-1-silenced CEM T cells exposed to CXCL12. F-actin content was measured by flow cytometry and is expressed relative to time zero. Data are presented as means ± SEM from three independent experiments; ***, $P < 0.001$ (by multifactorial ANOVA). (C) Representative images of F-actin (phalloidin, green), mitochondria (Mitotracker Orange, red), and ICAM-3 to mark the uropod (cyan) in maximum projections of a confocal Z-stack of CEM T cells plated on a matrix containing CXCL12. (D) Representative images of pMLC distribution in control and Miro-1-silenced CEM T cells plated on a CXCL12 matrix. Cells were stained for pMLC (green), Mitotracker Orange (red), and ERM (cyan). The graph shows pMLC fluorescence intensity ratios of the uropod and the leading edge. Data are shown as a scatter plot. Horizontal lines depict medians from two independent experiments; *, $P < 0.05$.

be involved in the confinement of mitochondria and MTOC at the contact zone.

The regulation of the interaction of mitochondria with the cytoskeleton is crucial for proper mitochondrial function at specific sites of action (6). In our search for a specific adaptor between mitochondria and microtubules, we focused on Miro-1, a member of the mitochondrial Rho GTPase family of proteins together with Miro-2. Our observations on Miro-2 expression levels suggest that Miro-1 plays unique functions in mitochondrial localization that cannot be replaced by Miro-2. Miro-1 localizes at the outer mitochondrial membrane and has two EF-hand $Ca^{2+}$ binding domains (13). Our data show, for the first time, that Miro-1 interacts with the dynein/dynactin complex, whereas interaction of Miro-1 with kinesin was previously described to promote anterograde mitochondrial movement (14, 15, 17, 18). This interaction may account for previously described effects on retrograde mitochondrial movement (48). In this regard, kinesin and dynein are interdependent in axonal transport (49), interacting directly through kinesin light chains (50) and indirectly through the same region of $p150^{glued}$ dynactin (51). These actions coordinate bidirectional movement of organelles along axon microtubules. Recent evidence suggests that kinesin and dynein can interact with the same mitochondrion, determining its complex mobility patterns in axons (52). Mitochondria can buffer the $Ca^{2+}$ that enters T lymphocytes via store-operated $Ca^{2+}$ channels (53). A recent study identified Miro-1 as a $Ca^{2+}$ sensor involved in the regulation of mitochondrial mobility in neurons and heart cell lines (16). Upon $Ca^{2+}$ binding to the EF-hand domains, a conformational change in Miro-1 provokes the release of mitochondria from microtubules and their arrest at the subcellular site of calcium influx, where they can contribute to the cell's response to this second messenger (15–17). Miro-1 function has been studied primarily in

**FIG 5** Miro-1 regulates cell polarity and mitochondrial relocalization to MTOC. (A) Left panel, quantification of elliptical form factor in control (1,213 cells) and Miro-1-silenced (1,245 cells) CEM T cells plated on a matrix containing CXCL12. Data are shown as a scatter plot. Horizontal lines depict medians from two independent experiments; ***, $P < 0.001$. Right panels, representative cells from each treatment group. Scale bars, 10 μm. (B) Quantification of elliptical form factor in CEM T cells overexpressing GFP (345 cells), GFP–Miro-1 (512 cells), and GFP-$Miro^{KK}$ (431 cells) and plated on a matrix containing CXCL12. Data are shown as a scatter plot. Horizontal lines depict medians from two independent experiments; *, $P < 0.05$. (C) 3D reconstruction of mitochondria (red) and MTOC (α-tubulin, green) in control and Miro-1-silenced CEM T cells plated on a matrix containing or lacking CXCL12. Scale bars, 2 μm. (D) Graph showing the distance between mitochondria and MTOC in cells as in panel C. Data are means ± SEM from two independent experiments; ***, $P < 0.001$ (by one-way ANOVA). The numbers of cells analyzed for each condition were 73 (siCrtl), 60 (CXCL12 siCtrl), 66 (siMiro), and 64 (CXCL12 siMiro). (E) 3D reconstruction of GFP proteins (green), mitochondria (red), and MTOC (α-tubulin, cyan) in CEM T cells overexpressing GFP, GFP–Miro-1, or GFP-$Miro^{KK}$ and plated on a matrix containing CXCL12. Scale bars, 2 μm. (F) Graph showing the distance between mitochondria and MTOC in cells as in panel D. The numbers of cells analyzed for each condition were 115 (GFP), 103 (GFP–Miro-1), and 113 (GFP-$Miro^{KK}$). Data are means ± SEM from two independent experiments (***, $P < 0.001$; **, $P < 0.01$).

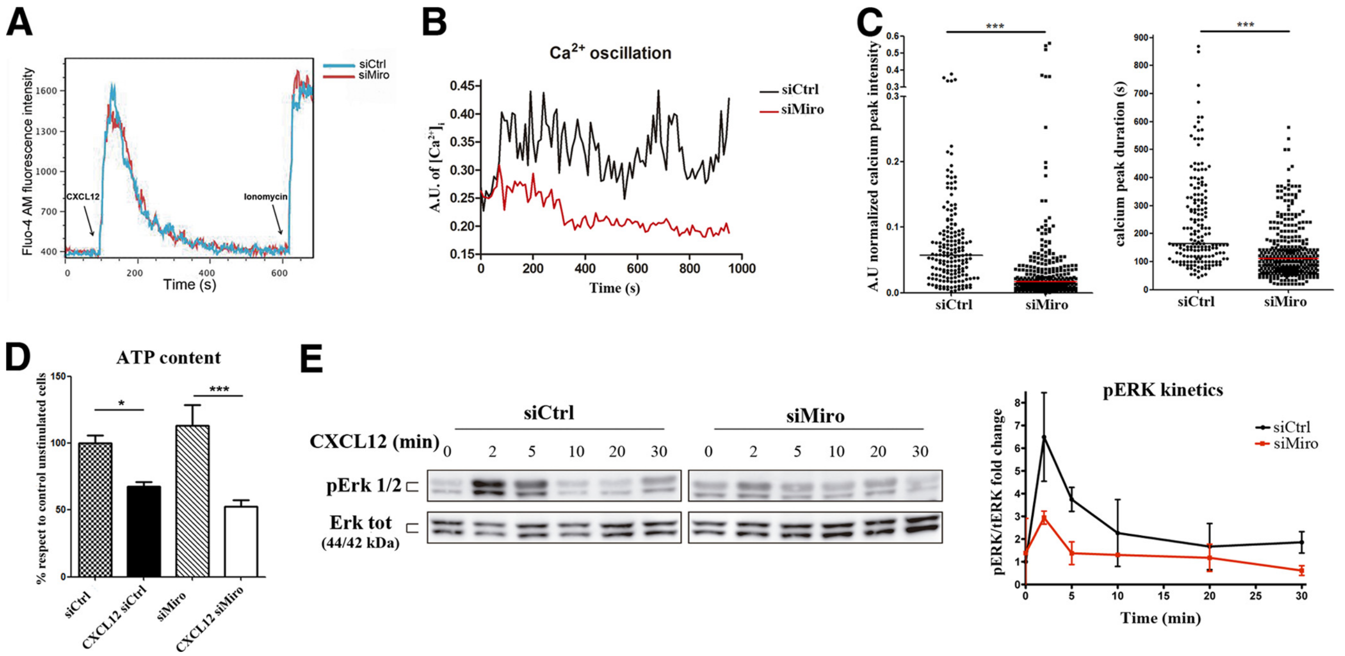

**FIG 7** Miro-1 regulates mitochondrion-dependent calcium influx during adhesion and migration. (A) Flow cytometry analysis of intracellular calcium dynamics (Fluo4-AM staining) in response to the addition of CXCL12 (10 nM) to a suspension of control and Miro-1-silenced CEM T cells (prestained with DiD and DiL, respectively). Results from a representative experiment out of three performed are shown. (B) Representative intracellular calcium oscillation in control and Miro-1-silenced CEM T cells migrating on TNF-α-activated HUVEC. (C) Distribution of relative calcium peak intensity (left) and peak duration in seconds (right). Data are shown as a scatter plot; horizontal lines depict medians from two independent experiments (67 control and 62 Miro-1-silenced cells) (***, $P < 0.001$). (D) Amounts of ATP in unstimulated and CXCL12-stimulated (10 min) control and Miro-1-intefered cells. Data are means ± SEM from two independent experiments. ***, $P < 0.001$; *, $P < 0.05$ (by one-way ANOVA). (E) Time course of the phosphorylation status of ERK1/2 in control and Miro-1-silenced CEM T cells activated with CXCL12. Total protein expression is shown as a loading control. The right panel shows pERK/total ERK band intensity ratios relative to the ratio in control cells at $t = 0$. Data are presented as the means ± SD from two independent experiments.

neuronal cells, where soma and synaptic structures can be distant from each other. It is therefore conceivable that mitochondrial positioning influences synaptic transmission by local ATP production and local $Ca^{2+}$ buffering. Although changes of mitochondrial positioning within small spherical cell like lymphocytes may be more modest (54), the evidence on how mitochondrial morphology and positioning are crucial for cellular signal threshold in immune cells is emerging (9–12, 43, 55). Our data demonstrate how changes of only few micrometers in lymphocyte mitochondrial positioning to the adhesion zone or to the uropod are able to significantly affect both adhesion and migration. Unlike lymphocytes, migrating epithelial cells require an anterior mitochondrial localization for correct migration. In these cells, Miro-1 knockdown also perturbs mitochondrial localization and reduces their migratory capability (56), in agreement with our data. The mitochondrial localization correlates with MTOC localization in leukocytes and epithelial cells (57, 58) and distribution of calcium levels (59).

In our model, the accumulation of mitochondria at the cell-to-cell contact suggests involvement of calcium in the polymerization and contraction of the actin cytoskeleton. This is in agreement with the defect in actin polymerization and in myosin light-chain phosphorylation found in Miro-1-silenced cells, correlating with the deficiency in mitochondrial polarization. These data suggest a possible function for the accumulation of mitochondria at the contact zone of the lymphocyte with the endothelium. Mitochondria may indeed supply the ATP necessary for the activity of the various kinases involved in these processes, as well as for actin polymerization and MLC phosphorylation required to establish and maintain persistent cell polarization. During firm adhesion, the combination of integrin signaling and exposure to immobilized chemokines on the apical surface of endothelial cells induces a marked change in the leukocyte morphology (60). Miro-1-silenced cells were unable to polarize properly under shear stress conditions, and these cells as well as $Miro^{KK}$-expressing cells showed impaired polarization in response to CXCL12 stimulation, highlighting the importance of Miro-1 in mitochondrial redistribution during cell polarization (61). These results indicate that $Ca^{2+}$ binding might dissociate Miro-1 from the dynein/dynactin complex, as previously described for kinesin interaction (15, 17). However, additional studies are required to demonstrate this.

The loss of mitochondrial accumulation around the MTOC in Miro-1-silenced cells upon CXCL12 stimulation was accompanied by impaired migration and transmigration, loss of directionality, reduced $Ca^{2+}$ oscillation during migration, and inhibition of ERK1/2 phosphorylation. It is therefore conceivable that Miro-1 regulates, through $Ca^{2+}$ binding to its EF motifs, the redistribution and relocation of mitochondria around the MTOC at the uropod, where they not only provide ATP to sustain actomyosin contraction (9) but also contribute to $Ca^{2+}$ influx at the rear of the migrating cell. The localized $Ca^{2+}$ influx may contribute, through calmodulin-based machinery, to the activation of the MLC kinase required for uropod retraction during migration (62, 63). At the same time, mitochondrial $Ca^{2+}$ influx can increase ATP production by activating the tricarboxylic acid cycle and enhancing the activities of the electron transport chain enzymes and the ATP synthase complex (64). Whether the impaired mitochondrial redistribution to the uropod caused by Miro-1 downregulation is able to reduce $Ca^{2+}$ entry at this subcellular location remains to be elucidated. Nevertheless, we cannot rule out that Miro-1 might play additional roles unrelated to mitochondrial positioning that might contribute to its effects on actin polymerization, calcium oscillations, and cell migration.

In summary, we demonstrate that Miro-1 can contribute to the regulation of mitochondrial translocation toward the MTOC during lymphocyte adhesion to the inflamed endothelium and the subsequent directed migration toward the site of inflammation, demonstrating the importance of mitochondrial subcellular localization in these processes. Considering the importance of an appropriate and rapid recruitment of leukocytes for an efficient immune response, our results shed new light about the regulation of adhesion and migration processes that could help the design of new, more specific strategies for the treatment of a large variety of immunological diseases in which there is deregulated leukocyte recruitment.

## ACKNOWLEDGMENTS

We thank S. Bartlett for English editing, Joseph T. Kittler for providing reagents, M. Vicente-Manzanares for critical reading of the manuscript, and V. Rocha-Perugini for helpful discussions. We thank the CNIC Microscopy and Celomics units.

This study was supported by SAF2011-25834 from the Spanish Ministry of Science and Innovation, INDISNET-S2011/BMD-2332 from the Comunidad de Madrid, Red Cardiovascular RD 12-0042-0056 from Instituto Salud Carlos III (ISCIII), and ERC-2011-AdG 294340-GENTRIS. J.M.G.-G. received salary support from the Miguel Servet (CP11/00145) ISCIII program. R.V.-B. was supported by a Juan de la Cierva postdoctoral contract from the Spanish Ministry of Economy and Competiveness (JCI-2011-09663).

## REFERENCES

1. **Barreiro O, de la Fuente H, Mittelbrunn M, Sanchez-Madrid F.** 2007. Functional insights on the polarized redistribution of leukocyte integrins and their ligands during leukocyte migration and immune interactions. Immunol. Rev. **218:**147–164. http://dx.doi.org/10.1111/j.1600-065X.2007.00529.x.
2. **Ley K, Laudanna C, Cybulsky MI, Nourshargh S.** 2007. Getting to the site of inflammation: the leukocyte adhesion cascade updated. Nat. Rev. Immunol. **7:**678–689. http://dx.doi.org/10.1038/nri2156.
3. **Kinashi T.** 2005. Intracellular signalling controlling integrin activation in lymphocytes. Nat. Rev. Immunol. **5:**546–559. http://dx.doi.org/10.1038/nri1646.
4. **Vicente-Manzanares M, Sanchez-Madrid F.** 2004. Role of the cytoskeleton during leukocyte responses. Nat. Rev. Immunol. **4:**110–122. http://dx.doi.org/10.1038/nri1268.
5. **Detmer SA, Chan DC.** 2007. Functions and dysfunctions of mitochondrial dynamics. Nat. Rev. Mol. Cell Biol. **8:**870–879. http://dx.doi.org/10.1038/nrm2275.
6. **Boldogh IR, Pon LA.** 2007. Mitochondria on the move. Trends Cell Biol. **17:**502–510. http://dx.doi.org/10.1016/j.tcb.2007.07.008.
7. **Li Z, Okamoto K, Hayashi Y, Sheng M.** 2004. The importance of dendritic mitochondria in the morphogenesis and plasticity of spines and synapses. Cell **119:**873–887. http://dx.doi.org/10.1016/j.cell.2004.11.003.
8. **Mattson MP, Gleichmann M, Cheng A.** 2008. Mitochondria in neuroplasticity and neurological disorders. Neuron **60:**748–766. http://dx.doi.org/10.1016/j.neuron.2008.10.010.
9. **Campello S, Lacalle RA, Bettella M, Manes S, Scorrano L, Viola A.** 2006. Orchestration of lymphocyte chemotaxis by mitochondrial dynamics. J. Exp. Med. **203:**2879–2886. http://dx.doi.org/10.1084/jem.20061877.
10. **Quintana A, Schwindling C, Wenning AS, Becherer U, Rettig J, Schwarz EC, Hoth M.** 2007. T cell activation requires mitochondrial translocation to the immunological synapse. Proc. Natl. Acad. Sci. U. S. A. **104:**14418–14423. http://dx.doi.org/10.1073/pnas.0703126104.
11. **Quintana A, Pasche M, Junker C, Al-Ansary D, Rieger H, Kummerow C, Nunez L, Villalobos C, Meraner P, Becherer U, Rettig J, Niemeyer BA, Hoth M.** 2011. Calcium microdomains at the immunological synapse: how ORAI channels, mitochondria and calcium pumps generate local calcium signals for efficient T-cell activation. EMBO J. **30:**3895–3912. http://dx.doi.org/10.1038/emboj.2011.289.
12. **Baixauli F, Martin-Cofreces NB, Morlino G, Carrasco YR, Calabia-Linares C, Veiga E, Serrador JM, Sanchez-Madrid F.** 2011. The mitochondrial fission factor dynamin-related protein 1 modulates T-cell receptor signalling at the immune synapse. EMBO J. **30:**1238–1250. http://dx.doi.org/10.1038/emboj.2011.25.
13. **Fransson A, Ruusala A, Aspenstrom P.** 2003. Atypical Rho GTPases have roles in mitochondrial homeostasis and apoptosis. J. Biol. Chem. **278:**6495–6502. http://dx.doi.org/10.1074/jbc.M208609200.
14. **Fransson S, Ruusala A, Aspenstrom P.** 2006. The atypical Rho GTPases Miro-1 and Miro-2 have essential roles in mitochondrial trafficking. Biochem. Biophys. Res. Commun. **344:**500–510. http://dx.doi.org/10.1016/j.bbrc.2006.03.163.
15. **Macaskill AF, Rinholm JE, Twelvetrees AE, Arancibia-Carcamo IL, Muir J, Fransson A, Aspenstrom P, Attwell D, Kittler JT.** 2009. Miro1 is a calcium sensor for glutamate receptor-dependent localization of mitochondria at synapses. Neuron **61:**541–555. http://dx.doi.org/10.1016/j.neuron.2009.01.030.
16. **Saotome M, Safiulina D, Szabadkai G, Das S, Fransson A, Aspenstrom P, Rizzuto R, Hajnoczky G.** 2008. Bidirectional Ca2+-dependent control of mitochondrial dynamics by the Miro GTPase. Proc. Natl. Acad. Sci. U. S. A. **105:**20728–20733. http://dx.doi.org/10.1073/pnas.0808953105.
17. **Wang X, Schwarz TL.** 2009. The mechanism of Ca2+-dependent regulation of kinesin-mediated mitochondrial motility. Cell **136:**163–174. http://dx.doi.org/10.1016/j.cell.2008.11.046.
18. **Glater EE, Megeath LJ, Stowers RS, Schwarz TL.** 2006. Axonal transport of mitochondria requires milton to recruit kinesin heavy chain and is light chain independent. J. Cell Biol. **173:**545–557. http://dx.doi.org/10.1083/jcb.200601067.
19. **Cai Q, Sheng ZH.** 2009. Moving or stopping mitochondria: Miro as a traffic cop by sensing calcium. Neuron **61:**493–496. http://dx.doi.org/10.1016/j.neuron.2009.02.003.
20. **Chang KT, Niescier RF, Min KT.** 2011. Mitochondrial matrix Ca2+ as an intrinsic signal regulating mitochondrial motility in axons. Proc. Natl. Acad. Sci. U. S. A. **108:**15456–15461. http://dx.doi.org/10.1073/pnas.1106862108.
21. **Yanez-Mo M, Alfranca A, Cabanas C, Marazuela M, Tejedor R, Ursa MA, Ashman LK, de Landazuri MO, Sanchez-Madrid F.** 1998. Regulation of endothelial cell motility by complexes of tetraspan molecules CD81/TAPA-1 and CD151/PETA-3 with alpha3 beta1 integrin localized at endothelial lateral junctions. J. Cell Biol. **141:**791–804. http://dx.doi.org/10.1083/jcb.141.3.791.
22. **Serrador JM, Alonso-Lebrero JL, del Pozo MA, Furthmayr H, Schwartz-Albiez R, Calvo J, Lozano F, Sanchez-Madrid F.** 1997. Moesin interacts with the cytoplasmic region of intercellular adhesion molecule-3 and is redistributed to the uropod of T lymphocytes during cell polarization. J. Cell Biol. **138:**1409–1423. http://dx.doi.org/10.1083/jcb.138.6.1409.
23. **Barreiro O, Yanez-Mo M, Serrador JM, Montoya MC, Vicente-Manzanares M, Tejedor R, Furthmayr H, Sanchez-Madrid F.** 2002. Dynamic interaction of VCAM-1 and ICAM-1 with moesin and ezrin in a novel endothelial docking structure for adherent leukocytes. J. Cell Biol. **157:**1233–1245. http://dx.doi.org/10.1083/jcb.200112126.
24. **Cereghetti GM, Stangherlin A, Martins de Brito O, Chang CR, Blackstone C, Bernardi P, Scorrano L.** 2008. Dephosphorylation by calcineurin regulates translocation of Drp1 to mitochondria. Proc. Natl. Acad. Sci. U. S. A. **105:**15803–15808. http://dx.doi.org/10.1073/pnas.0808249105.
25. **Martin-Cofreces NB, Robles-Valero J, Cabrero JR, Mittelbrunn M, Gordon-Alonso M, Sung CH, Alarcon B, Vazquez J, Sanchez-Madrid F.** 2008. MTOC translocation modulates IS formation and controls sustained T cell signaling. J. Cell Biol. **182:**951–962. http://dx.doi.org/10.1083/jcb.200801014.
26. **Campanero MR, del Pozo MA, Arroyo AG, Sanchez-Mateos P, Hernandez-Caselles T, Craig A, Pulido R, Sanchez-Madrid F.** 1993. ICAM-3 interacts with LFA-1 and regulates the LFA-1/ICAM-1 cell adhesion pathway. J. Cell Biol. **123:**1007–1016. http://dx.doi.org/10.1083/jcb.123.4.1007.
27. **Barreiro O, Zamai M, Yanez-Mo M, Tejera E, Lopez-Romero P, Monk PN, Gratton E, Caiolfa VR, Sanchez-Madrid F.** 2008. Endothelial adhe-

sion receptors are recruited to adherent leukocytes by inclusion in preformed tetraspanin nanoplatforms. J. Cell Biol. **183:**527–542. http://dx.doi.org/10.1083/jcb.200805076.

28. **Martin-Cofreces NB, Baixauli F, Lopez MJ, Gil D, Monjas A, Alarcon B, Sanchez-Madrid F.** 2012. End-binding protein 1 controls signal propagation from the T cell receptor. EMBO J. **31:**4140–4152. http://dx.doi.org/10.1038/emboj.2012.242.
29. **de la Fuente H, Mittelbrunn M, Sanchez-Martin L, Vicente-Manzanares M, Lamana A, Pardi R, Cabanas C, Sanchez-Madrid F.** 2005. Synaptic clusters of MHC class II molecules induced on DCs by adhesion molecule-mediated initial T-cell scanning. Mol. Biol. Cell **16:**3314–3322. http://dx.doi.org/10.1091/mbc.E05-01-0005.
30. **Vicente-Manzanares M, Cabrero JR, Rey M, Perez-Martinez M, Ursa A, Itoh K, Sanchez-Madrid F.** 2002. A role for the Rho-p160 Rho coiled-coil kinase axis in the chemokine stromal cell-derived factor-1alpha-induced lymphocyte actomyosin and microtubular organization and chemotaxis. J. Immunol. **168:**400–410.
31. **Vicente-Manzanares M, Viton M, Sanchez-Madrid F.** 2003. Measurement of the levels of polymerized actin (F-actin) in chemokine-stimulated lymphocytes and GFP-coupled cDNA transfected lymphoid cells by flow cytometry. Methods Mol. Biol. **239:**53–68. http://dx.doi.org/10.1385/1-59259-435-2:53.
32. **Villa-Bellosta R, Wang X, Millan JL, Dubyak GR, O'Neill WC.** 2011. Extracellular pyrophosphate metabolism and calcification in vascular smooth muscle. Am. J. Physiol. Heart Circ. Physiol. **301:**H61–68. http://dx.doi.org/10.1152/ajpheart.01020.2010.
33. **Herreros L, Rodriguez-Fernandez JL, Brown MC, Alonso-Lebrero JL, Cabanas C, Sanchez-Madrid F, Longo N, Turner CE, Sanchez-Mateos P.** 2000. Paxillin localizes to the lymphocyte microtubule organizing center and associates with the microtubule cytoskeleton. J. Biol. Chem. **275:**26436–26440. http://dx.doi.org/10.1074/jbc.M003970200.
34. **Karki S, Holzbaur EL.** 1999. Cytoplasmic dynein and dynactin in cell division and intracellular transport. Curr. Opin. Cell Biol. **11:**45–53. http://dx.doi.org/10.1016/S0955-0674(99)80006-4.
35. **Lammermann T, Bader BL, Monkley SJ, Worbs T, Wedlich-Soldner R, Hirsch K, Keller M, Forster R, Critchley DR, Fassler R, Sixt M.** 2008. Rapid leukocyte migration by integrin-independent flowing and squeezing. Nature **453:**51–55. http://dx.doi.org/10.1038/nature06887.
36. **del Pozo MA, Sanchez-Mateos P, Nieto M, Sanchez-Madrid F.** 1995. Chemokines regulate cellular polarization and adhesion receptor redistribution during lymphocyte interaction with endothelium and extracellular matrix. Involvement of cAMP signaling pathway. J. Cell Biol. **131:**495–508.
37. **Harada A, Takei Y, Kanai Y, Tanaka Y, Nonaka S, Hirokawa N.** 1998. Golgi vesiculation and lysosome dispersion in cells lacking cytoplasmic dynein. J. Cell Biol. **141:**51–59. http://dx.doi.org/10.1083/jcb.141.1.51.
38. **Bleul CC, Fuhlbrigge RC, Casasnovas JM, Aiuti A, Springer TA.** 1996. A highly efficacious lymphocyte chemoattractant, stromal cell-derived factor 1 (SDF-1). J. Exp. Med. **184:**1101–1109. http://dx.doi.org/10.1084/jem.184.3.1101.
39. **Miller KE, Sheetz MP.** 2004. Axonal mitochondrial transport and potential are correlated. J. Cell Sci. **117:**2791–2804. http://dx.doi.org/10.1242/jcs.01130.
40. **Lee CW, Peng HB.** 2008. The function of mitochondria in presynaptic development at the neuromuscular junction. Mol. Biol. Cell **19:**150–158. http://dx.doi.org/10.1091/mbc.E07-05-0515.
41. **Teicher BA, Fricker SP.** 2010. CXCL12 (SDF-1)/CXCR4 pathway in cancer. Clin. Cancer Res. **16:**2927–2931. http://dx.doi.org/10.1158/1078-0432.CCR-09-2329.
42. **Suzuki Y, Rahman M, Mitsuya H.** 2001. Diverse transcriptional response of CD4(+) T cells to stromal cell-derived factor (SDF)-1: cell survival promotion and priming effects of SDF-1 on CD4(+) T cells. J. Immunol. **167:**3064–3073.
43. **Contento RL, Campello S, Trovato AE, Magrini E, Anselmi F, Viola A.** 2010. Adhesion shapes T cells for prompt and sustained T-cell receptor signalling. EMBO J. **29:**4035–4047. http://dx.doi.org/10.1038/emboj.2010.258.
44. **Liu S, Thomas SM, Woodside DG, Rose DM, Kiosses WB, Pfaff M, Ginsberg MH.** 1999. Binding of paxillin to alpha4 integrins modifies integrin-dependent biological responses. Nature **402:**676–681. http://dx.doi.org/10.1038/45264.
45. **Schaller MD.** 2001. Paxillin: a focal adhesion-associated adaptor protein. Oncogene **20:**6459–6472. http://dx.doi.org/10.1038/sj.onc.1204786.
46. **Hsia DA, Lim ST, Bernard-Trifilo JA, Mitra SK, Tanaka S, den Hertog J, Streblow DN, Ilic D, Ginsberg MH, Schlaepfer DD.** 2005. Integrin alpha4beta1 promotes focal adhesion kinase-independent cell motility via alpha4 cytoplasmic domain-specific activation of c-Src. Mol. Cell. Biol. **25:**9700–9712. http://dx.doi.org/10.1128/MCB.25.21.9700-9712.2005.
47. **Rodriguez-Fernandez JL, Sanchez-Martin L, de Frutos CA, Sancho D, Robinson M, Sanchez-Madrid F, Cabanas C.** 2002. LFA-1 integrin and the microtubular cytoskeleton are involved in the Ca(2)(+)-mediated regulation of the activity of the tyrosine kinase PYK2 in T cells. J. Leukoc. Biol. **71:**520–530.
48. **Russo GJ, Louie K, Wellington A, Macleod GT, Hu F, Panchumarthi S, Zinsmaier KE.** 2009. Drosophila Miro is required for both anterograde and retrograde axonal mitochondrial transport. J. Neurosci. **29:**5443–5455. http://dx.doi.org/10.1523/JNEUROSCI.5417-08.2009.
49. **Martin M, Iyadurai SJ, Gassman A, Gindhart JG, Jr, Hays TS, Saxton WM.** 1999. Cytoplasmic dynein, the dynactin complex, and kinesin are interdependent and essential for fast axonal transport. Mol. Biol. Cell **10:**3717–3728. http://dx.doi.org/10.1091/mbc.10.11.3717.
50. **Ligon LA, Tokito M, Finklestein JM, Grossman FE, Holzbaur EL.** 2004. A direct interaction between cytoplasmic dynein and kinesin I may coordinate motor activity. J. Biol. Chem. **279:**19201–19208. http://dx.doi.org/10.1074/jbc.M313472200.
51. **Deacon SW, Serpinskaya AS, Vaughan PS, Lopez Fanarraga M, Vernos I, Vaughan KT, Gelfand VI.** 2003. Dynactin is required for bidirectional organelle transport. J. Cell Biol. **160:**297–301. http://dx.doi.org/10.1083/jcb.200210066.
52. **Cai Q, Davis ML, Sheng ZH.** 2011. Regulation of axonal mitochondrial transport and its impact on synaptic transmission. Neurosci. Res. **70:**9–15. http://dx.doi.org/10.1016/j.neures.2011.02.005.
53. **Hoth M, Fanger CM, Lewis RS.** 1997. Mitochondrial regulation of store-operated calcium signaling in T lymphocytes. J. Cell Biol. **137:**633–648. http://dx.doi.org/10.1083/jcb.137.3.633.
54. **Junker C, Hoth M.** 2011. Immune synapses: mitochondrial morphology matters. EMBO J. **30:**1187–1189. http://dx.doi.org/10.1038/emboj.2011.72.
55. **Abarca-Rojano E, Muniz-Hernandez S, Moreno-Altamirano MM, Mondragon-Flores R, Enriquez-Rincon F, Sanchez-Garcia FJ.** 2009. Re-organization of mitochondria at the NK cell immune synapse. Immunol. Lett. **122:**18–25. http://dx.doi.org/10.1016/j.imlet.2008.10.008.
56. **Desai SP, Bhatia SN, Toner M, Irimia D.** 2013. Mitochondrial localization and the persistent migration of epithelial cancer cells. Biophys. J. **104:**2077–2088. http://dx.doi.org/10.1016/j.bpj.2013.03.025.
57. **del Pozo MA, Nieto M, Serrador JM, Sancho D, Vicente-Manzanares M, Martinez C, Sanchez-Madrid F.** 1998. The two poles of the lymphocyte: specialized cell compartments for migration and recruitment. Cell Adhes. Commun. **6:**125–133. http://dx.doi.org/10.3109/15419069809004468.
58. **Yvon AM, Walker JW, Danowski B, Fagerstrom C, Khodjakov A, Wadsworth P.** 2002. Centrosome reorientation in wound-edge cells is cell type specific. Mol. Biol. Cell **13:**1871–1880. http://dx.doi.org/10.1091/mbc.01-11-0539.
59. **Brundage RA, Fogarty KE, Tuft RA, Fay FS.** 1993. Chemotaxis of newt eosinophils: calcium regulation of chemotactic response. Am. J. Physiol. **265:**C1527–1543.
60. **Sanchez-Madrid F, del Pozo MA.** 1999. Leukocyte polarization in cell migration and immune interactions. EMBO J. **18:**501–511. http://dx.doi.org/10.1093/emboj/18.3.501.
61. **Gomez-Mouton C, Manes S.** 2007. Establishment and maintenance of cell polarity during leukocyte chemotaxis. Cell Adhes. Migr. **1:**69–76. http://dx.doi.org/10.4161/cam.1.2.4547.
62. **Eddy RJ, Pierini LM, Matsumura F, Maxfield FR.** 2000. Ca2+-dependent myosin II activation is required for uropod retraction during neutrophil migration. J. Cell Sci. **113:**1287–1298.
63. **Clark AJ, Petty HR.** 2008. Observation of calcium microdomains at the uropod of living morphologically polarized human neutrophils using flash lamp-based fluorescence microscopy. Cytometry A **73:**673–678. http://dx.doi.org/10.1002/cyto.a.20580.
64. **Jouaville LS, Pinton P, Bastianutto C, Rutter GA, Rizzuto R.** 1999. Regulation of mitochondrial ATP synthesis by calcium: evidence for a long-term metabolic priming. Proc. Natl. Acad. Sci. U. S. A. **96:**13807–13812. http://dx.doi.org/10.1073/pnas.96.24.13807.